

Engineering Characteristics of Ground Motions Recorded in the 2019 Ridgecrest Earthquake Sequence

Sean Kamran Ahdi^{*1,2}, Silvia Mazzoni³, Tadahiro Kishida⁴, Pengfei Wang³, Chukwuebuka C. Nweke³, Nicolas M. Kuehn³, Victor Contreras³, Badie Rowshandel⁵, Jonathan P. Stewart³, and Yousef Bozorgnia³

ABSTRACT

We present a database and analyze ground motions recorded during three events that occurred as part of the July 2019 Ridgecrest earthquake sequence: a moment magnitude (M) 6.5 foreshock on a left-lateral cross fault in the Salt Wells Valley fault zone, an M 5.5 foreshock in the Paxton Ranch fault zone, and the M 7.1 mainshock, also occurring in the Paxton Ranch fault zone. We collected and uniformly processed 1483 three-component recordings from an array of 824 sensors spanning 10 seismographic networks. We developed site metadata using available data and multiple models for the time-averaged shear-wave velocity in the upper 30 m (V_{S30}) and for basin depth terms. We processed ground motions using Next Generation Attenuation (NGA) procedures and computed intensity measures including spectral acceleration at a number of oscillator periods and inelastic response spectra. We compared elastic and inelastic response spectra to seismic design spectra in building codes to evaluate the damage potential of the ground motions at spatially distributed sites. Residuals of the observed spectral accelerations relative to the NGA-West2 ground-motion models (GMMs) show good average agreement between observations and model predictions (event terms between about -0.3 and 0.5 for peak ground acceleration to 5 s). The average attenuation with distance is also well captured by the empirical NGA-West2 GMMs, although azimuthal variations in attenuation were observed that are not captured by the GMMs. An analysis considering directivity and fault-slip heterogeneity for the M 7.1 event demonstrates that the dispersion in the near-source ground-motion residuals can be reduced.

KEY POINTS

- We developed a database of ground-motion recordings from three events in the Ridgecrest earthquake sequence.
- We find good average agreement between observed spectral accelerations and ground-motion model predictions.
- The dataset is available as a tool for researchers and practitioners to use in future ground-motion studies.

INTRODUCTION

The 4 July 2019 Ridgecrest earthquake sequence started at 10:33 a.m. local time, with a moment magnitude (M) 6.5 event located south of China Lake and west of Searles Valley, California (Fig. 1). This M 6.5 event occurred on a left-lateral north-east-trending fault (roughly parallel with the Garlock fault to the south) at a hypocentral depth of 10.5 km. This earthquake was followed on 5 July by an M 5.5 event at 4:07 a.m. local time at a hypocentral depth of 7.0 km, and an M 7.1 event at 8:19 p.m.

local time, the latter on a northwest-trending right-lateral fault at a depth of 8.0 km (Geotechnical Extreme Event Reconnaissance [GEER], 2019). These events occurred on faults within the formerly named greater Little Lake fault zone, but have now been differentiated after the recent earthquakes and are referred to as the Salt Wells Valley fault zone (for the M 6.5 event; Dawson *et al.*, 2020) and the Paxton Ranch fault zone (for the M 7.1 event; Dawson *et al.*, 2020). Because they

1. Exponent, Inc., Los Angeles, California, U.S.A.; 2. Department of Earth, Planetary, and Space Sciences, University of California, Los Angeles, Los Angeles, California, U.S.A.; 3. Department of Civil and Environmental Engineering, University of California, Los Angeles, Los Angeles, California, U.S.A.; 4. Department of Civil Infrastructure and Environmental Engineering, Khalifa University of Science and Technology, Abu Dhabi, United Arab Emirates; 5. California Earthquake Authority (CEA), Sacramento, California, U.S.A.

*Corresponding author: sahdi@ucla.edu

Cite this article as Ahdi, S. K., S. Mazzoni, T. Kishida, P. Wang, C. C. Nweke, N. M. Kuehn, V. Contreras, B. Rowshandel, J. P. Stewart, and Y. Bozorgnia (2020). Engineering Characteristics of Ground Motions Recorded in the 2019 Ridgecrest Earthquake Sequence, *Bull. Seismol. Soc. Am.* **110**, 1474–1494, doi: [10.1785/B120200036](https://doi.org/10.1785/B120200036)

© Seismological Society of America

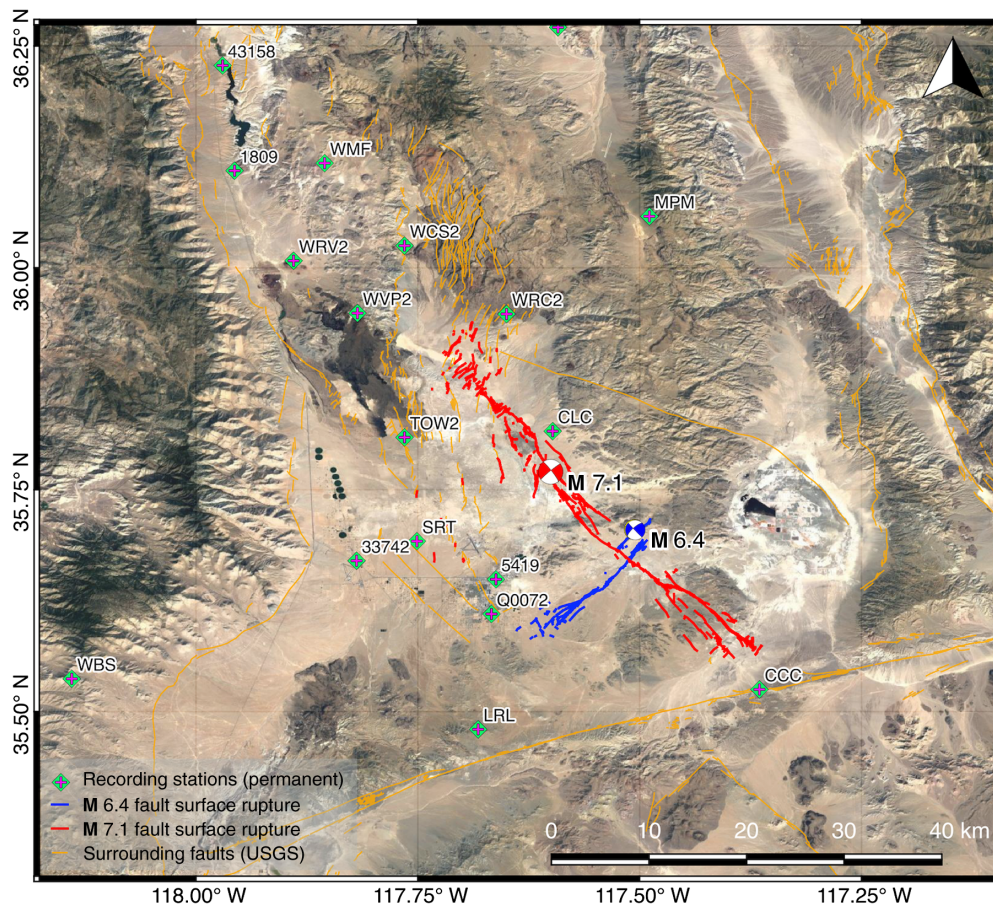


Figure 1. Regional map including epicentral locations of Ridgecrest earthquake sequence mainshocks, mapped Quaternary faults, and strong-motion recording stations. USGS, U.S. Geological Survey. The color version of this figure is available only in the electronic edition.

were proximal in space and time, the $M 6.5$ and $M 5.5$ events are considered to be foreshocks to the $M 7.1$ event. The moment magnitudes of these three earthquakes are taken from the Global Centroid Moment Tensor (Global CMT) catalog, as presented in the [Seismic Source Parameters](#) section.

The Ridgecrest earthquake sequence was the largest to originate within southern California in 20 yr, since the 1999 $M 7.1$ Hector Mine earthquake. The number of recording stations in the region has grown significantly during this time period. The Pacific Earthquake Engineering Research Center Next Generation Attenuation (NGA)-West2 ground-motion database presents 131 records for the Hector Mine event ([Ancheta et al., 2013](#)), much fewer than the 747 records of the largest event in the Ridgecrest sequence described herein. As ground-motion databases grow, methods to organize, store, and query such data have evolved as well. Data presented in this study are organized into a relational database (RDB) with a structure that is scalable, allows data attributes to be associated with recorded data, and allows for more efficient data querying. The RDB structure from NGA-Subduction, as described by [Mazzoni et al. \(2020\)](#), was adopted for the present study. Data are also presented in

traditional flatfile format, emulating the main products from the past NGA projects.

In this article, we present recorded and processed ground motions, independent (measured) metadata, including information describing the recording stations (site), and dependent (computed) data and metadata, such as various source-to-site distance metrics and directivity parameters, and computed elastic and inelastic response spectra. We also investigate near-source effects, including spatial variations of ground-motion amplitudes, and directivity and heterogeneity effects of the $M 7.1$ mainshock. We present results of a residuals analysis that was performed to assess the predictive power of the five NGA-West2 shallow crustal ground-motion models (GMMs) for the three main events of the Ridgecrest earthquake sequence. All data are publicly available from the University of California, Los Angeles Natural Hazards Risk and Resiliency Research Center, as described in [Ahdi et al. \(2019\)](#).

RECORDED GROUND MOTIONS

A total of 824 strong-motion recording stations from 10 seismographic networks recorded ground motions from the Ridgecrest earthquake sequence. A breakdown of stations by network is presented in [Ahdi et al. \(2019\)](#). Figure 2 shows the spatial distribution of the recording stations in the source region. Although the earthquakes occurred in a remote area of the Mojave Desert, there were 30 stations that recorded the $M 7.1$ mainshock located within 100 km of its epicenter, with one station (CLC) located only 5 km to the north. The U.S. Geological Survey (USGS) undertook a rapid deployment of an array of 19 seismic instruments to record aftershocks starting two days after the mainshock ([Cochran et al., 2020](#)); these data were not included in this study, primarily because such smaller magnitude aftershocks generally do not produce strong ground motion of engineering interest.

Table 1 summarizes basic attributes of the three main events in the sequence and the number of recorded ground motions

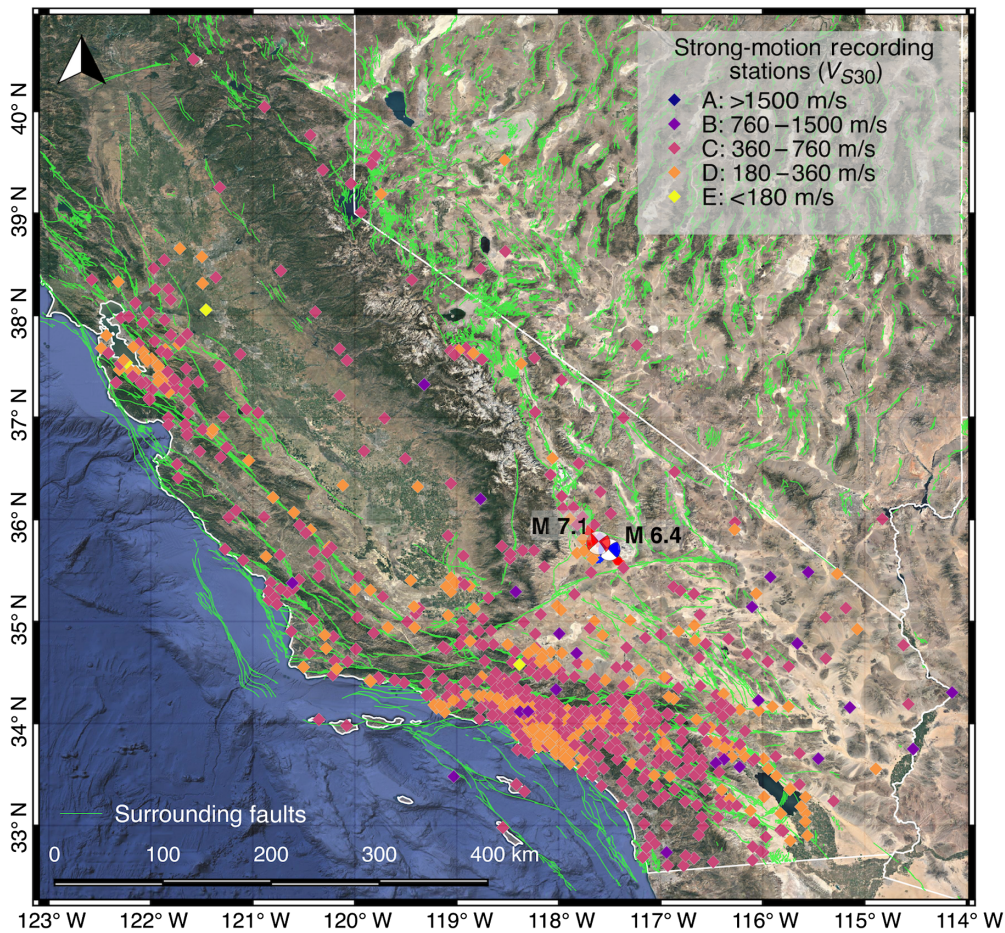


Figure 2. Spatial distribution of recording stations in the ground motion database. Stations are color-shaded according to V_{S30} -based National Earthquake Hazards Reduction Program site class. The color version of this figure is available only in the electronic edition.

for each event. In total, the database includes 1483 three-component recordings, that is, 4449 individual records. Recordings were downloaded from the Center for Engineering Strong-Motion Data (CESMD, see [Data and Resources](#)). Recordings are sequentially labeled with a record sequence number 1–1483. All ground motions were processed according to the procedures described in the NGA-Subduction Project ([Kishida et al., 2020](#)), which includes digital signal processing of the

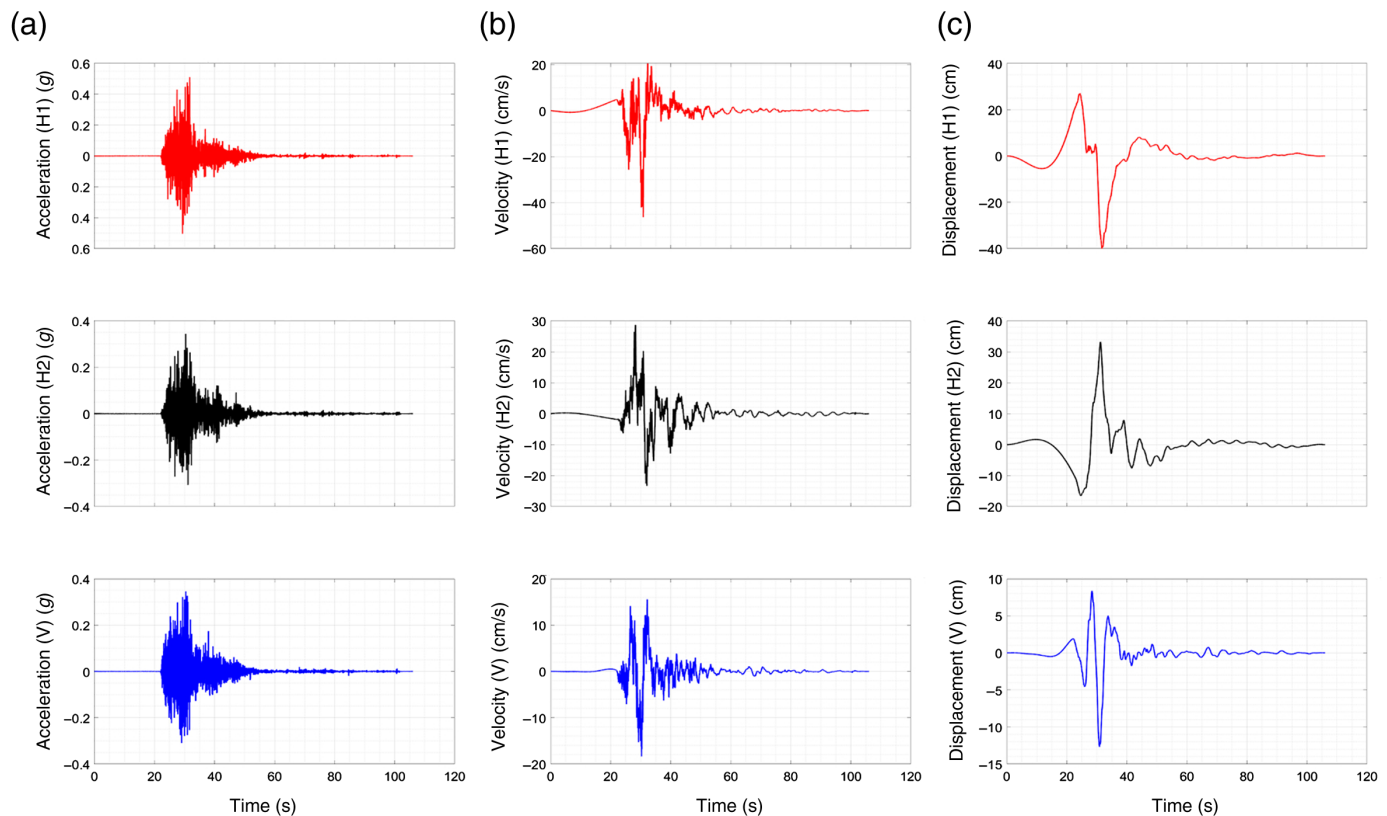
raw recordings for noise removal, baseline correction, computation of velocity and displacement time series, and computation of various response spectral ordinates. The three components (two horizontal and one vertical) of accelerations recorded at station CLC during the M 7.1 earthquake, along with the computed velocity and displacement traces, are shown in Figure 3. A larger number of recordings were originally obtained before a vetting process following standard NGA protocols ([Ancheta et al., 2013](#); [Goulet et al., 2014](#); [Kishida et al., 2016](#)) removed some from inclusion in the final database. Time series for sensors located on structures, such as dam crests or building basements, were excluded from the database. During data processing, time series were inspected for record quality by checking *P*- and *S*-wave arrival times against event origin times and hypocentral distances. Records having very poor signal quality (i.e., signal-to-noise ratio <3) were rejected. Time series with *P*- and *S*-wave arrival times that vary significantly from the expected arrival times, such as if an *S*-wave arrival is not recorded due to late triggering, or if the observed *P*-wave duration is significantly different from the expected value based on the hypocentral distance, were also excluded from the database. Overall, approximately 10% of the total records were rejected.

TABLE 1
Summary of Events and Number of Recordings Included in the Database

Event-Magnitude	Date (yyyy/mm/dd) and Time of Event*	Epicentral Latitude (°N) [†]	Epicentral Longitude (°W) [†]	Hypocentral Depth (km) [†]	Number of Recording Stations	Number of Recordings
M 6.5	2019/07/04, 10:33:49 a.m.	35.705	117.504	10.5	527	1581
M 5.5	2019/07/05, 4:07:53 a.m.	35.760	117.575	7.0	209	627
M 7.1	2019/07/05, 8:19:53 p.m.	35.770	117.599	8.0	747	2241

*Local date and time (Pacific Daylight time).

[†]Source: U.S. Geological Survey (USGS) event pages.



Twenty-two stations were located at close rupture distance (<21 km) of the causative faults. Data recorded at these stations were rotated into fault-normal (FN) and fault-parallel (FP) components. The spectra for these rotated records were computed and compared to the other components to determine whether ground-motion polarization can be observed (further discussion in the [Ground-Motion Intensity Measures](#) section).

COMPILATION OF METADATA

Seismological parameters such as magnitude, style of faulting, and fault geometry were reviewed and compiled to facilitate ground-motion studies, including calculation of distance metrics. The following subsections elaborate on the computation of distances and estimation of site parameters for recording sites.

Seismic source parameters

Seismic moments and resulting moment magnitudes were taken from the Global CMT project ([Ekström et al., 2012](#)). We prefer these magnitudes, because they are well constrained from data derived from global seismic networks. The use of Global CMT magnitudes conforms with NGA procedures, as described by [Contreras et al. \(2020\)](#).

We reviewed two finite-fault solutions for each of the **M** 6.5 and **M** 7.1 events available from the Finite-Fault Earthquake Source Model Database (also known as SRCMOD, [Mai and Thingbaijam, 2014](#)). These models were developed by [Xu et al. \(2020\)](#), denoted here as Xff) and [Ross et al. \(2019\)](#), denoted here

Figure 3. Example plots of the **M** 7.1 event ground motions for site CLC: (a) processed recorded acceleration, (b) computed velocity, and (c) computed displacement time series for the two horizontal (H1 and H2) and vertical (V) components. The color version of this figure is available only in the electronic edition.

as Rff). Each of the two sets of models were developed using satellite data obtained from Interferometric Synthetic Aperture Radar, while Rff also utilized relocated aftershock seismicity, near-field and teleseismic waveforms, and geodetic observations to constrain the models. Xff provided a single rectangular fault model for the **M** 6.5 event, and a seven-rectangle-segmented fault model for the **M** 7.1 event. Rff provided a complex, multifault model for the entire Ridgecrest earthquake sequence by manually inferring surface fault traces from the analysis of geodetic data, resulting in a complex network of interlaced orthogonal faults, and connecting these to a vertical segment below 5 km with appropriately dipping segments to constrain the model to deeper seismicity.

For the **M** 5.5 event, we estimated a finite-fault representation of the earthquake rupture using a simulation procedure that provides a rectangular fault geometry. This procedure was originally developed in the NGA-West1 Project by [Chiou and Youngs \(2008\)](#) and coded in FORTRAN as the script “CCLD.” The procedures were updated for NGA-Sub (revised script is named “CCLD5”) and is documented in more detail by [Contreras et al. \(2020\)](#). As applied in the present study, the procedure takes as input the hypocentral location

TABLE 2

Trimmed Finite-Fault Model Parameters for the M 6.5 and M 7.1 Earthquakes after Xu et al. (2020) and Estimated Source Parameters of the M 5.5 Earthquake

Event	Seismic Moment M_0 (dyn-cm)*	Moment	Hypocentral Latitude (°)	Hypocentral Longitude (°)	Hypocentral Depth (km)	Number of Fault Model Segments	L (km)	W (km)	Z_{TOR} (km)	Strike (°)	Dip (°)	Rake (°)
		Magnitude (M)										
M 6.5	5.95×10^{25}	6.48	35.6341	-117.550	9.78	1	12.76	14.51	0.00	225.57	90	-5.18
M 5.5	1.77×10^{24}	5.47	35.7600	-117.575	7.00	1	5.54	3.74	4.4	315	75	-150
M 7.1	4.39×10^{26}	7.06	35.7710 [†]	-117.5965 [†]	8.00	5	46.50	20.00	0.00	134.79	90	173.22

Z_{TOR} , depth to top of rupture.

*Seismic moment from the Global Centroid Moment Tensor (Global CMT) catalog was preferred.

[†]The hypocentral location was slightly modified to make it consistent with the trimmed fault plane.

(Table 1) and the orientation of the preferred nodal plane (strike and dip; taken from Global CMT). The approximate geometry (along-strike length L and down-dip width W) was obtained from simulations by means of area (A) and aspect ratio (L/W) relationships conditioned on the magnitude of the event, whereas the down-dip position of the hypocenter on the fault plane was obtained from simulations conditioned on the mechanism of the event (in this case, strike slip).

For the M 6.5 and M 7.1 events, we follow the procedure described by Contreras et al. (2020) to trim finite-fault models (FFMs) and remove regions where the slip is less than 15% of the maximum slip associated with the rupture of each event. Xff requires less geometric modification for conversion to a single rectangular fault (i.e., for the ground-surface projections of the M 6.5 FFMs) or contiguously connected rectangular fault segments (i.e., for the ground-surface projections of the M 7.1 FFMs). Therefore, we selected Xff as the model applied for source–site distance calculations. The Xff FFM for the M 7.1 event was simplified to five continuously connected rectangular fault segments for the purpose of trimming and distance calculations. The resultant source parameters based on the trimmed Xff FFMs and the statistically simulated fault plane for the M 5.5 event are presented in Table 2.

Distance metrics

Several site-to-source distance metrics are provided in the database for each recording, including hypocentral distance R_{HYP} , epicentral distance R_{EPI} , Joyner–Boore distance R_{JB} (closest distance from site to any point on the surface

projection of the fault surface), rupture distance R_{RUP} (closest distance from site to any point on the fault surface), R_X (distance measured perpendicular to the fault strike from the surface projection of the up-dip edge of the fault plane), R_Y (distance measured parallel to the fault strike from the midpoint of the surface projection of the fault plane), and R_{Y0} (distance measured parallel to the fault strike from the end of the surface projection of the fault plane).

Distance metrics were computed using the FORTRAN code “P4CF” (Contreras et al., 2020). The inputs required by this code are the 3D representation of the ruptured fault plane of each event and the locations of the ground motion stations. The fault associated with each event is represented by one or more rectangles (inferred from the trimmed FFMs or generated using statistical simulations), each of which is located by geodetic coordinates and depth of the upper corners of the rectangle, strike, dip, and down-dip width. R_{RUP} and R_{JB} for individual recording stations were identical for both the M 6.5 and M 7.1 events, because both FFMs extend from depth up to the ground surface and have vertical (90°) dips.

Site metadata

A site database (SDB) was developed, encompassing information such as (where available for each station) network code, station location information (latitude, longitude, and elevation), information on the time-averaged shear-wave velocity (V_S) in the upper 30 m (V_{S30}) obtained from both measured V_S profiles and from proxy-based estimates, and basin depth parameters (z_x), which are measured as the vertical distance from the ground surface to the first encounter of $x = 1.0$, 1.5, and 2.5 km/s V_S horizons.

V_{S30} values at recording stations. A map of all stations in the SDB is presented in Figure 2, and the markers are color-coded based on National Earthquake Hazards Reduction Program site classes associated with the assigned V_{S30} value. V_{S30} values were assigned based on the availability of measured V_S profiles from geophysical measurements proximate (<300 m) to the recording station. When measured V_{S30} values are unavailable, V_{S30} is assigned based on various proxy-based

TABLE 3

Breakdown of Data Sources for Measured V_{S30} Data

Data Source	Number of Measurements
U.S. Community V_S profile database	158
Center for Engineering Strong-Motion Data (CESMD)	25
NGA-West2 site database (SDB)	20
Total	203

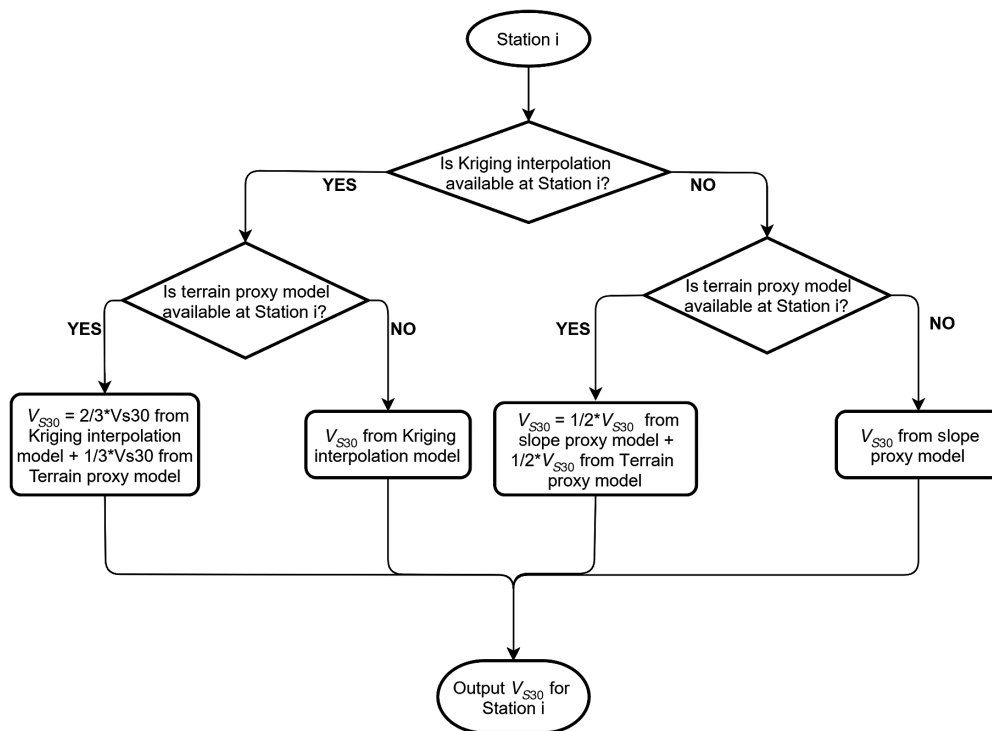


Figure 4. Flowchart depicting logic for assignments for proxy-based V_{S30} values in absence of measurements within proximity to station. Note that the geo model (hybrid geology-slope proxy model of [Wills et al., 2015](#)) was not considered on its own, as it is a basis for the map used in the Kriging-based model of [Thompson \(2018\)](#).

models, including those based on surficial geology, topographic slope, and geomorphic terrain classifications. The following protocol was used in assigning V_{S30} values for a given station:

1. Consider available published databases of measured V_S profiles and V_{S30} values:
 - United States Community V_S profile database (PDB, [Ahdi et al., 2018](#)), which includes data from the USGS V_{S30} compilation ([Yong et al., 2016](#))
 - NGA-West2 SDB ([Seyhan et al., 2014](#))
 - CESMD (2019)
2. Match available measured V_{S30} values from all databases to station of interest by computing the distances between the station and the locations of the V_{S30} measurement, and, take the closest measurement (using a 300 m cutoff distance), if there are multiple available measurements that do not match the station coordinates exactly (i.e., distance = 0 m).
3. Use proxy-based V_{S30} estimation models if:
 - a. There exists no V_{S30} measurement within 300 m of the station; or
 - b. The only measured V_{S30} within 300 m of the station was obtained using the refraction microtremor (ReMi) method ([Louie, 2001](#)).

We exclude V_{S30} values obtained using the ReMi method, primarily due to potential bias toward higher phase velocities

when omnidirectional noise sources are not present, as shown in past studies (e.g., [Cox and Beekman, 2011](#); [Strobbia and Cassiani, 2011](#)).

The SDB includes 824 recording stations. A total of 203 (25%) stations have measured V_{S30} values, and for the remaining 621 stations, V_{S30} values are inferred using proxy-based methods (described in the following). For stations with measured V_{S30} , breakdown by original data source is provided in [Table 3](#).

For sites lacking *in situ* V_{S30} measurements, one or more of the following proxy-based models was utilized:

1. krig: a Kriging-based regression map informed by measured V_{S30} data and a hybrid geology-topographic slope model. The Kriging approach is from [Thompson et al. \(2014\)](#) and [Thompson \(2018\)](#), and the hybrid model is from [Wills et al. \(2015\)](#);
2. terr: geomorphic terrain proxy model ([Yong, 2016](#)) based on terrain classes from [Iwahashi and Pike \(2007\)](#); and
3. slp: topographic slope-based model ([Wald and Allen, 2007](#)).

To compute the model output, all sites in the SDB were assigned the relevant values of terrain classes or topographic slope gradients or were plotted on the raster map for the krig model. [Figure 4](#) illustrates the assignment of V_{S30} based on these parameters. The krig model is preferred due to its inclusion of measured V_{S30} values and thus is utilized wherever data falls within the geographic extent of the model (i.e., the state of California). Weights of 2/3 and 1/3 were applied for sites using both the krig and terr models, respectively. All inferred V_{S30} values from proxy-based models used the krig or krig-terr pair of models, except for 10 sites located in Nevada for which the kriging map is not defined, and one site (CGS station number 13877) that plots in water.

Assignment of basin depth parameters. The z_x parameters were obtained by querying the Unified Community Velocity Models (CVMs) provided by the Southern California Earthquake Center ([Small et al., 2017](#)). Values were obtained by querying a metamodel, which is a tiled system of multiple

TABLE 4

Seismic Velocity Models Registered into the Unified Community Velocity Model (UCVM, after [Small et al., 2017](#); [Nweke et al., 2018](#))

UCVM Model Name and Abbreviation	Description	Region, Coverage Coordinates	References
SCEC CVM-H, v.15.1 (cvmh)	3D velocity model defined on regular mesh, no geotechnical layer. Based on 3D tomographic inversions of seismic reflection profiles and direct velocity measurements from boreholes	Southern California; –120.8620, 30.9565; –113.3329, 30.9565; –113.3329, 36.6129; –120.8620, 36.6129	Süss and Shaw (2003) ; Shaw et al. (2015)
SCEC CVM-S4 (cvms)	3D velocity model defined as rule-based system with a geotechnical layer. Uses query of velocity by depth using empirical relationships from borehole sonic logs and tomographic studies	Irregular area in Southern California	Kohler et al. (2003)
SCEC CVM-S4.26 (cvms5)	3D velocity model defined on regular mesh, no geotechnical layer. Uses query of velocity by depth based on CVM-S4 as starting model, improved using full 3D tomography	Southern central California, southern California; –116.0000, 30.4499; –122.3000, 34.7835; –118.9475, 38.3035; –112.5182, 33.7819	Lee et al. (2014)
SCEC CVM-S4.26.M01, (cvmsi)	3D velocity model defined on regular mesh with query by depth that adds a GTL to CVM-S4.26		
USGS Hi-res and Lo-res etree v.08.3.0, (cencal)	3D velocity model defined on regular mesh with geotechnical layer that uses velocity query by depth	San Francisco Bay Area, North and central California; –126.3532, 39.6806; –123.2732, 41.4849; –118.9445, 36.7022; –121.9309, 35.0090	Brocher et al. (2006)
Central California model, SCEC CCA06, (cca)	3D tomographic inversions done on a coarse mesh (500 m), trilinear interpolation between nodes	Central California; –122.9362, 36.5298; –118.2678, 39.3084; –115.4353, 36.0116; –120.0027, 33.3384	Still in beta; Chen and Lee (2017)
SCEC CS17.3, (cs173)	CyberShake 17.3 velocity model with added geotechnical layer (UCVMC18.5)	Central California; –127.6187, 37.0453; –124.5299, 41.3799–112.9435, 35.2956; –116.4796, 31.2355	Still in beta; Ely et al. (2010) ; 2016
SCEC CS17.3-H (cs173h)	17.3 model integrated with Harvard Santa Maria and San Joaquin basin models with geotechnical layer		
Modified Hadley and Kanamori (1d) Northridge region (bbp1d)	1D velocity model in nine layers that defines V_p and scaling relationship for V_s . Nonbasin areas 1D velocity model defined in 18 layers, derived from velocity profiles at SCSN stations. Nonbasin areas.	Southern California, irregular boundary Northridge region, irregular boundary	Hauksson (2010) Graves and Pitarka (2010)

SCEC, Southern California Earthquake Center; SCSN, Southern California Seismic Network.

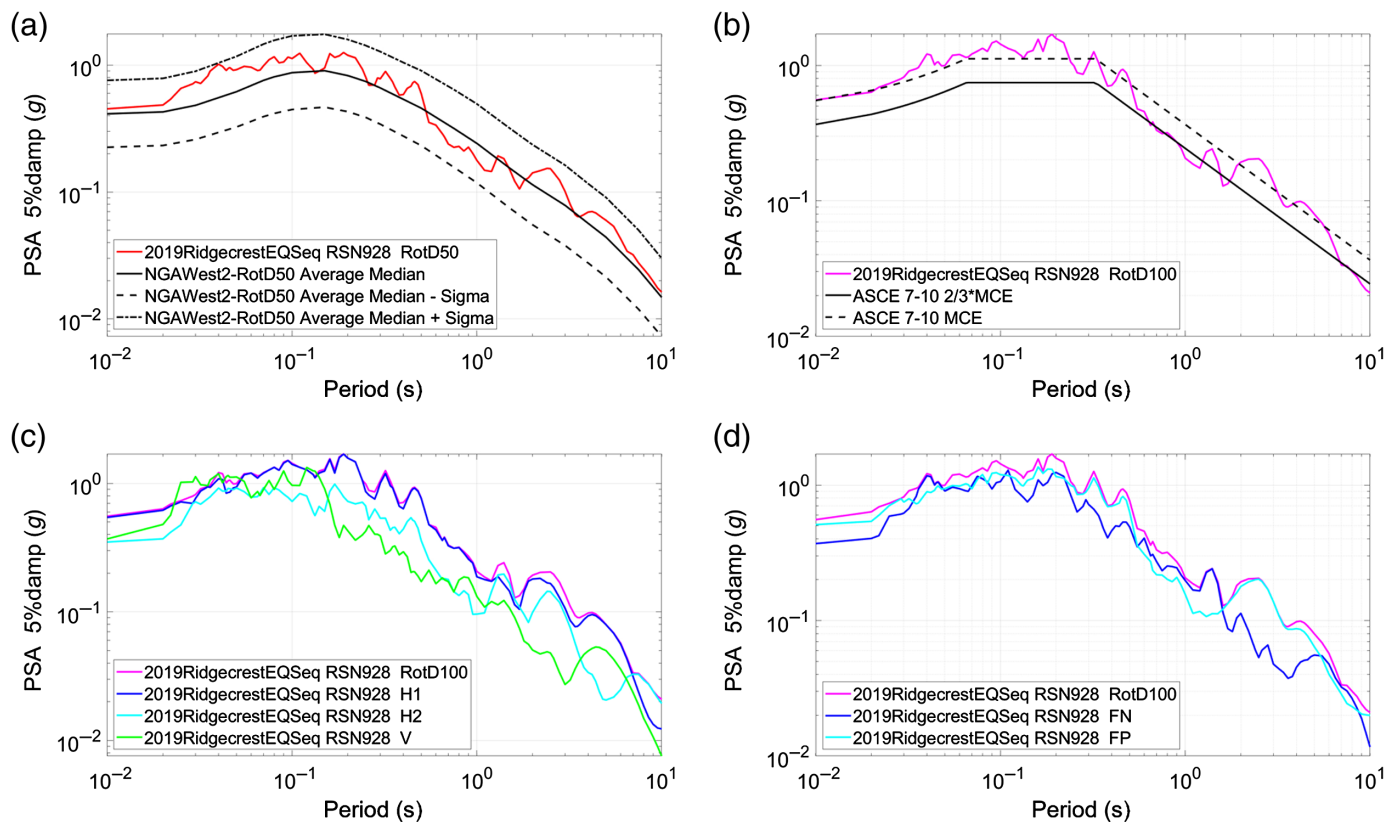
velocity models. For this project, the metamodel consisted of five velocity models. The order of the velocity models in the metamodel was based on the extent of geographical coverage as follows: cvmsi, cencal, cs173h, cca, and 1d. These acronyms are explained and elaborated upon in Table 4. The cvmsi and cvmh are two of the prominent velocity models for the southern California region, with both CVMs covering similar geographical extents. However, cvmsi was preferred over cvmh for this project's metamodel, because an evaluative study by [Taborda et al. \(2016\)](#) shows that cvmsi yields stronger goodness of fit for simulated ground motions.

The tiled system uses latitude and longitude coordinates to query the CVMs in order of their designated priority. If the coordinates fall within the geographical extents of a model, then the appropriate z_x value will be selected ([Small et al., 2017](#)). If the coordinate falls outside the geographical extents of the given model, the next CVM in the tiled order will be checked, and the process is repeated until a CVM is

encountered that encompasses the location of interest. To account for locations outside the boundary region of the velocity models in the metamodel, a background 1d velocity model is placed last in the tiled structure, as it covers the largest area and serves as a supporting model to the standard CVMs. If a site's coordinates were to fall outside of all tiled CVM extents, the site is not assigned a z_x value. For this dataset, all 827 stations fell within the extent of the tiled CVMs and were thus assigned z_x values. When the model output for a site yields $z_{1.0} = 0$, we check against geological maps. Zero depth is retained for sites located on mapped hard rock geology (crystalline rock, Cretaceous rock, or volcanic rock units), and $z_{1.0}$ is indicated as undefined if the geology is mapped as tertiary rock or sediments.

GROUND-MOTION INTENSITY MEASURES

Elastic response spectra were computed for the time series collected for the three main events, including the three individual



as-recorded components (H1, H2, and V), the RotD50 and RotD100 components, and the FP and FN components of the records in the vicinity of the faults. RotD50 and RotD100 are defined by Boore (2010). Figure 5 shows an example of these intensity measures for the site CLC located 2 km from the M 7.1 rupture, as compared to GMMs and code-based values. Figure 5a compares the RotD50 component to predictions from the NGA-West2 GMMs for the 16th, 50th (median), and 84th percentiles (also for RotD50); this comparison is discussed in detail in the [Comparisons with NGA-West2 GMMs](#) section. Figure 5b compares the RotD100 component to the American Society of Civil Engineers (ASCE) 7-10 mapped design values—the risk-targeted maximum considered earthquake, MCE_R , and the design earthquake DE ($DE = 2/3 \cdot MCE_R$), adjusted for its site class (ASCE, 2010). This comparison shows that the M 7.1 Ridgecrest mainshock exceeded the design-earthquake spectrum at this location for most structural periods. Figure 5c compares the response spectrum of the three as-recorded components to the maximum component (RotD100). The H1 horizontal direction has the highest spectral demand for all periods. Figure 5d compares the response spectra for the FP and FN components to the maximum component shown in Figure 5c. At this location, the FP component carries most of the energy at long periods, which is contrary to the expectation that the FN component generally has larger spectral ordinates at longer periods (Somerville, 2002). These rotated

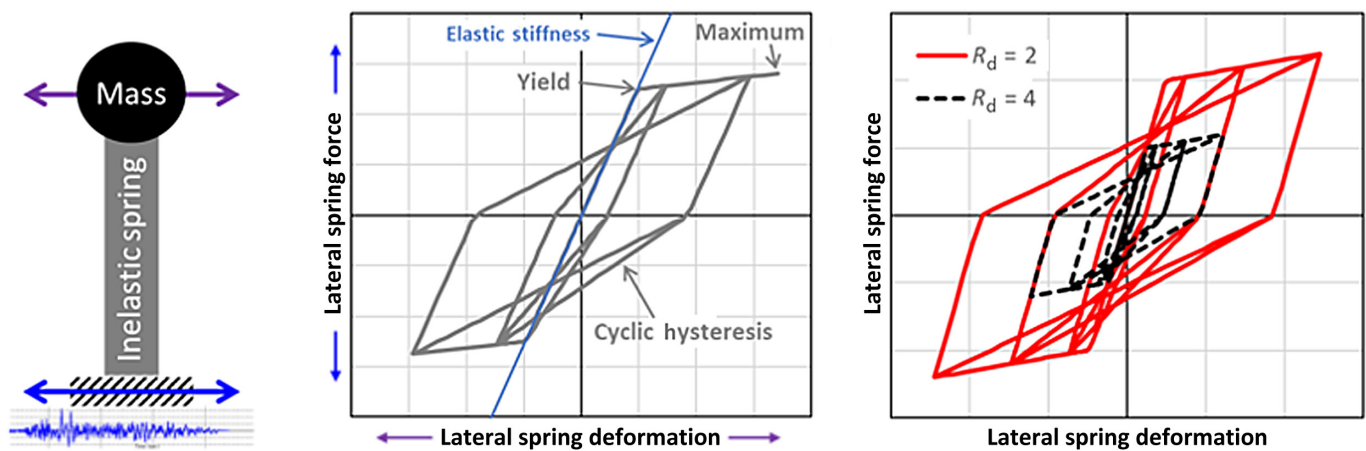
Figure 5. Example plots from the M 7.1 event for site CLC of (a) observed RotD50 response spectrum compared with the average of the five Next Generation Attenuation (NGA)-West2 predictions; (b) observed RotD100 response spectrum as compared with the American Society of Civil Engineers (ASCE) 7–10 risk-targeted maximum considered earthquake (MCE_R) spectrum and design earthquake ($DE = 2/3 \cdot MCE_R$) spectrum; (c) observed RotD100, H1, H2, and V response spectra; and (d) observed RotD100, fault-normal (FN), and fault-parallel (FP) response spectra. PSA, pseudospectral acceleration. The color version of this figure is available only in the electronic edition.

components are valuable to studies of near-fault effects and provide insight on ground-motion polarization.

Spatial distribution of damage potential

ShakeMaps provided by the USGS (Worden and Wald, 2016) provide a geographic representation of ground shaking, as represented by elastic response spectra. These maps show pseudospectral acceleration (PSA) at particular periods using a combination of instrument recordings and GMMs. Because PSA is related to the peak response of an elastic oscillator, it can be a good measure of seismic demand for elastic structures. However, it does not account for structural yielding, which is an expected phenomenon for structures subjected to strong motions.

On the other hand, nonlinear time-dependent analyses of representative structure types using the recorded ground



motions provide an opportunity to draw different insights into the geographic distribution of expected inelastic structural response and damage potential in the area affected by the seismic event. These analyses were performed on a generalized inelastic single-degree-of-freedom (SDOF) model using the finite-element framework OpenSees (McKenna *et al.*, 2010). The main feature of an inelastic model is its ability to capture strength reduction and softening due to yielding, as well hysteretic energy dissipation due to cyclic loading and ductility. Thus, the two main features of inelastic structural response, effective period elongation due to yielding and hysteretic energy dissipation, are accounted for. The variable characteristics of the model are its elastic stiffness, hence its period, and the strength parameter, which defines the yield point (strength and deformation). A graphical representation of the SDOF analysis model is shown in Figure 6. Because both horizontal instrument recordings were available for each site, the SDOF model shown was implemented in 2D using an axisymmetric structural element. For this case, the yield deformation is the same for all rotation angles (θ). Such a system is often referred to as a coupled system because the behavior (strength) in one direction is affected by the deformation in the orthogonal direction.

The strength parameter that was used in the analysis is the estimated strength-reduction factor (R_d), defined as the ratio between the lateral-force strength for design and the yield strength of the structure, V_y . This value is equivalent to a combination of the strength-reduction factor R and the overstrength factor used in seismic structural design. The typical range for R_d is between 0.5 and 4. When $R_d = 1$, the structure will yield at the DE level. When $R_d > 1$, the structure will yield when subjected to a below-design-level earthquake. When $R_d < 1$, the structure will remain elastic at and below the DE. Most structures are defined with an $R_d > 1$. It is important to note that with this definition of R_d the estimated yield strength of the structure is defined as a function of the design spectrum at the site. The ASCE 7–10 MCE_R spectrum (ASCE, 2010) was obtained for each recording station via the USGS Design Maps Web Services tools (see Data and Resources).

Figure 6. Graphical representation of single-degree-of-freedom (SDOF) analysis model. The color version of this figure is available only in the electronic edition.

Either the ASCE 7–10 standard or ASCE 7–16 specification (ASCE, 2016) could be used; we used the former as it does not require site-specific analyses for softer soil conditions, which would prevent uniform application of the current methodology to all recording stations presented herein. A graphical representation of the effect of R_d on the yielding oscillator response is shown in Figure 6. Two values of R_d were chosen for the analyses ($R_d = 2$ and 4). These values are expected to represent structures designed to an R-factor between 4 and 8 (assuming the strength achieved in structures is twice that used in design, i.e., overstrength of 2.0). Inelastic response values were computed for two periods (0.2 and 1.0 s). The yield displacement, or deformation, defined by the yield strength (corresponding to R_d) divided by the elastic stiffness (corresponding to T , the oscillator period) defines the elastic-deformation limit (D_y) for each model.

The inelastic and elastic responses of the 2D SDOF system were computed for all the recordings for the M 7.1 event for both periods and strength levels. The maximum-deformation response was extracted for each analysis. Figure 7 shows an example of the hysteretic response of the elastic and inelastic systems as well as the deformation trace in the two horizontal directions. For the elastic case, a damping ratio of 5% was used, which is common in engineering practice. For the inelastic case, a reduced damping ratio of 2% was utilized, as the hysteretic energy dissipation is already captured in these nonlinear analyses as compared to the elastic case, which leverages a higher viscous damping ratio to partly capture the hysteretic damping that is not explicitly modeled therein.

For each inelastic case ($R_d = 2$ and 4, and $T = 0.2$ and 1.0 s) at each recording station, the maximum deformation was normalized by the elastic-deformation limit. This ratio can be considered a good measure of the damage potential,

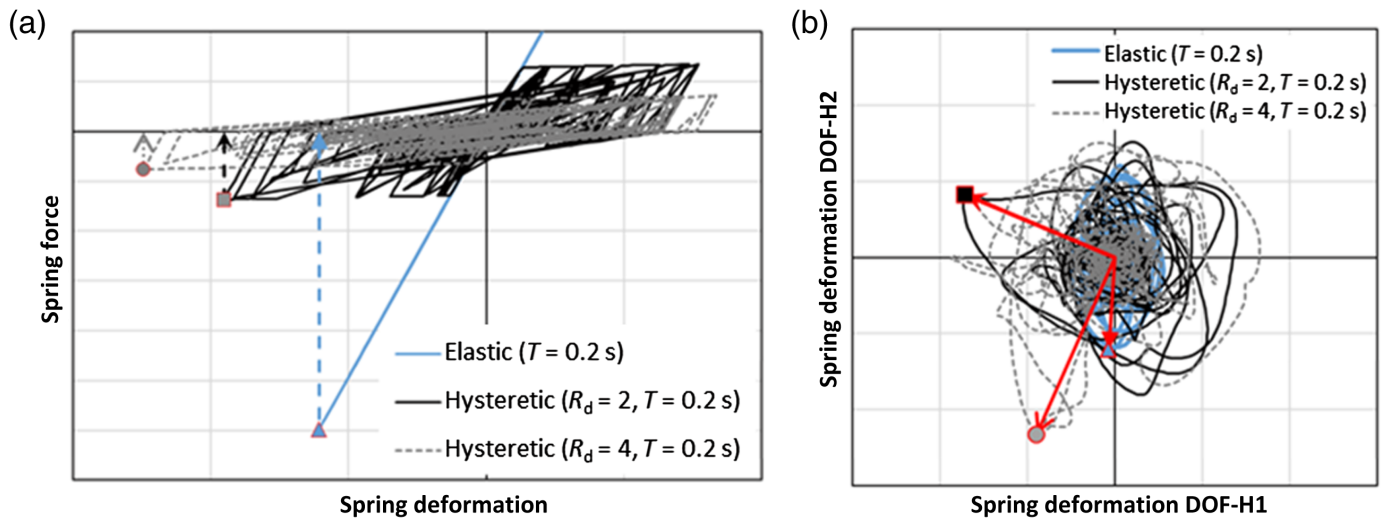


Figure 7. Representative response of 2D SDOF (a) elastic and (b) inelastic systems. The color version of this figure is available only in the electronic edition.

because it quantifies whether the structure has yielded and the level of inelastic demands beyond the elastic limit. These quantities are mapped for $T = 1.0$ s oscillators in Figure 8 for $R_d = 2$ and in Figure 9 for $R_d = 4$. Each figure consists of four maps. The first map (Figs. 8a and 9a) shows the geographic distribution of the maximum elastic-deformation demand (S_d). This map is the equivalent of a ShakeMap, because the maximum elastic deformation and the spectral acceleration are proportional by a factor that is only a function of period. The data in this map are the same for both cases of R_d . The second map (Figs. 8b and 9b) plots the geographic distribution of D_y , which is defined by expected strength evaluated from the R_d factor and the ASCE 7–10 MCE spectra. Zones of high seismicity, such as those near the San Andreas fault that runs approximately northwest–southeast across the center of the map, are expected to be designed for higher deformation limits. Structures designed with $R_d = 2$ have higher deformation limits than those designed with $R_d = 4$, by definition, a factor of 2. The maps in Figures 8c and 9c show the geographic distribution of the inelastic-deformation demands (D_{max}). Because of the significant distance from the earthquake source, the maximum-deformation demand of the two strength cases is the same because the system remains elastic in most cases. Hence, the data shown in the last set of maps (Figs. 8d and 9d) normalize deformation demands by the elastic limit, providing a better representation of the relationship between demands and capacities in terms of the elastic-deformation limit.

The normalized deformation demands (Figs. 8d and 9d) show that there are different regions with different levels of expected response, both near and far from the epicenter. The patterns shown in the damage potential maps indicate that distance and site conditions are not the only response parameters. Validation of these results would entail comparisons to locations of damaged structures, a database of which has not been released to our knowledge. The limited information

currently available (e.g., GEER, 2019, section 2.5) indicates impacts to highly vulnerable structures in Ridgecrest and Trona (e.g., unbraced mobile homes), but overall good structural performance outside of the military base. Damage within the Naval Air Weapons Station China Lake, where damage potential maps indicate $D_{max}/D_y > \sim 2$, has been anecdotally described as relatively severe in some cases (M. Boggs, U.S. Navy, personal comm., 2019), but specific information about the location of these structures and the extent of their damage is not publicly available.

In summary, the data shown in Figures 8 and 9 are consistent with the observed distribution of damage: most of the damage concentrated in the regions near the fault trace, such as Ridgecrest and Trona. These regions have high damage potential values in the map.

Comparisons with NGA-West2 GMMs

Using the metadata associated with each event and station, the median, 16th, and 84th percentile predictions of RotD50 ground motions were computed for the five NGA-West2 GMMs. Figure 5a shows an example for the M 7.1 event at site CLC.

Residuals (difference between RotD50 from data and GMM median) were calculated with respect to the five NGA-West2 models: Abrahamson *et al.* (2014), Boore *et al.* (2014), Campbell and Bozorgnia (2014), Chiou and Youngs (2014), and Idriss (2014) (hereafter, ASK, BSSA, CB, CY, and ID, respectively). The residuals were calculated at periods $T = 0.01, 0.02, 0.03, 0.05, 0.075, 0.1, 0.15, 0.2, 0.25, 0.3, 0.4, 0.5, 0.75, 1.0, 1.5, 2.0, 3.0, 4.0, 5.0, 7.5,$ and 10.0 s. For each GMM and period, we

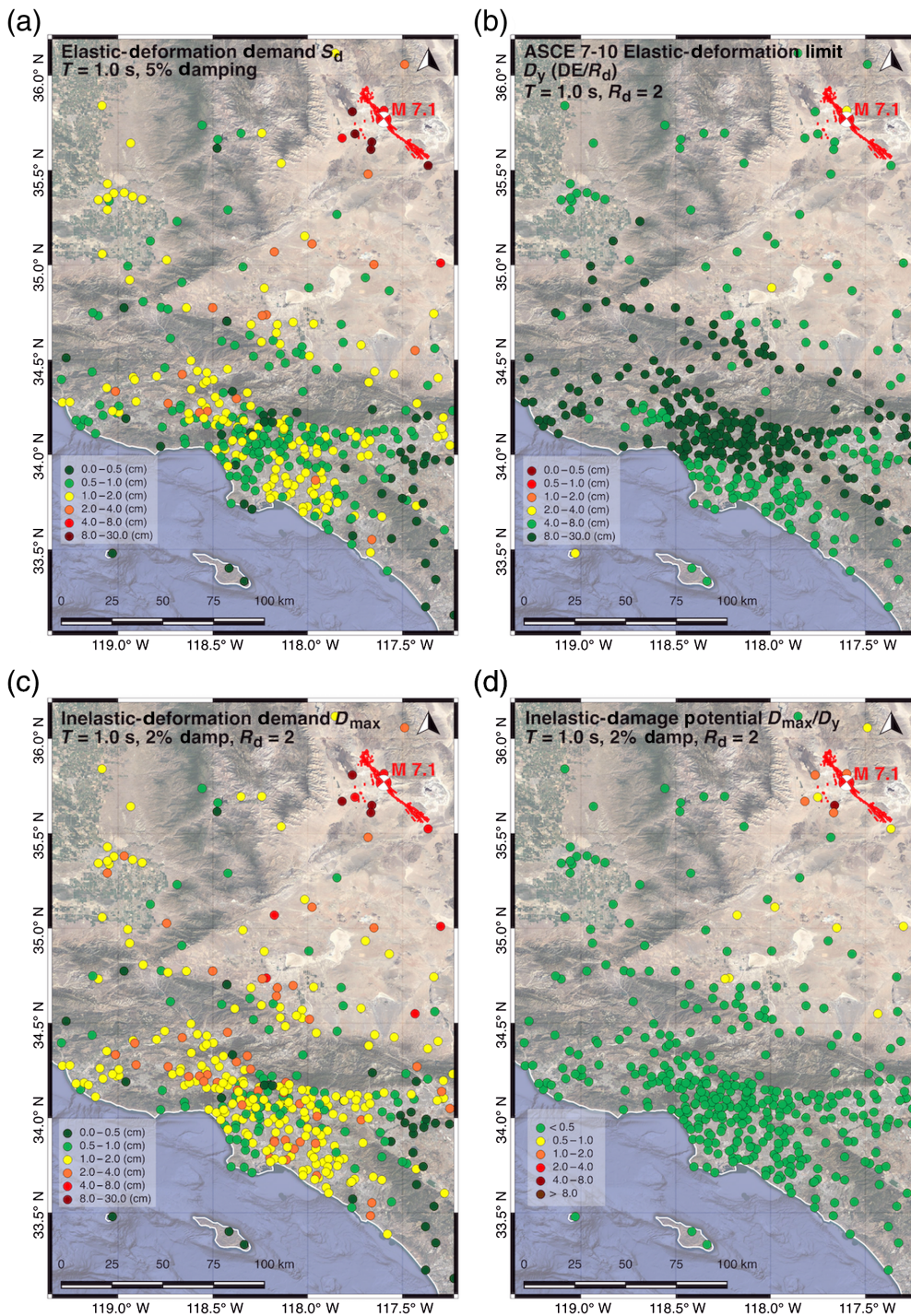


Figure 8. Peak deformation response of single-degree-of-freedom oscillators with elastic period, $T = 1.0$ s: (a) elastic case, 5% damping; (b) ASCE 7-10 elastic deformation limit $D_y(DE/R_d)$, $R_d = 2$; (c) inelastic deformation demand, D_{max} , $R_d = 2$, 2% damping; (d) inelastic-damage potential (D_{max}/D_y), $R_d = 2$, 2% damping. The color version of this figure is available only in the electronic edition.

calculate the average residual for rupture distances (R_{RUP}) < 300 km and V_{S30} between 150 and 1500 m/s for ASK, BSSA, CB, CY; and $R_{RUP} < 150$ km, and $450 < V_{S30} < 1200$ for ID. The average residual can be taken as an event term

for well-recorded events for which path and distance scaling are well captured by the GMM. As shown subsequently, there are some biases in these scaling relationships for the GMMs, so the average residual is not equivalent to an event term.

Figure 10a–c shows average residuals for all three events, which are slightly positive for the two larger events at short periods (ranging between -0.05 and 0.29 at $T = 0.01$ s). The M 5.5 event shows a larger range of average residuals between the models, a reflection of the larger between-model variability at lower magnitudes for the NGA-West2 models. At longer periods, average residuals increase, perhaps due to underprediction of basin depth scaling by the GMMs. Figure 11a,b shows the trend of total residuals of all events for the ASK and CY GMMs, respectively, for PSA at $T = 1.0$ s versus $z_{1.0}$. Residuals increase for deeper $z_{1.0}$ values.

Average residuals of the M 5.5 event at long periods increase more strongly with distance than for the other events. This feature in the results is likely caused by path effects associated with these events and the distribution of recording stations. Figure 12a, b shows maps of the full residuals for the BSSA GMM at $T = 3.0$ s, with stations color coded by the value of the residual. The spatial distributions of residuals for both the M 5.5 and M 7.1 events show similar trends, with strong positive residuals to the west and smaller residuals to the south-southeast. The M 7.1 event is recorded by more stations in the south-southeast, which affects the average residual for the events.

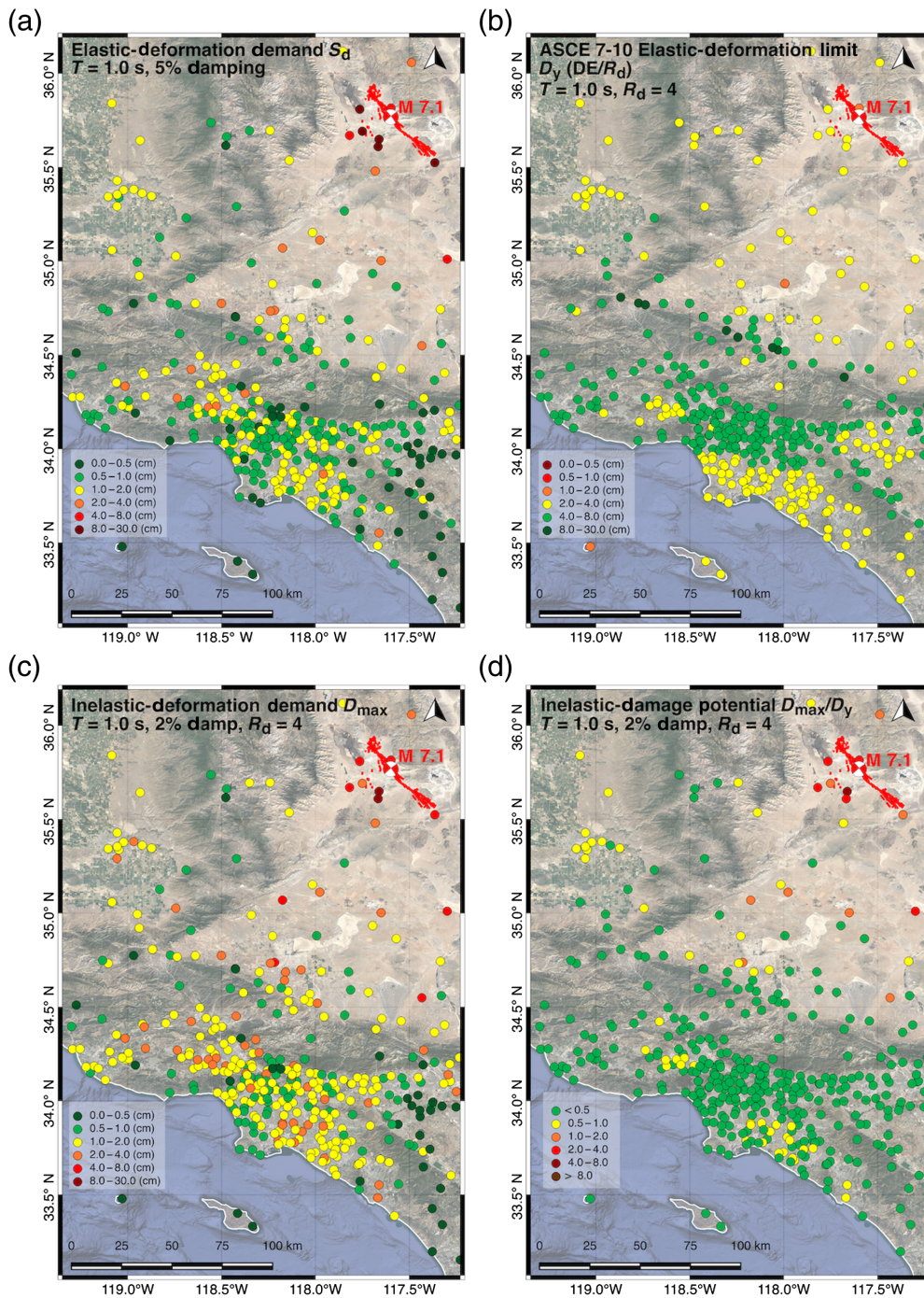


Figure 9. Peak deformation response of single-degree-of-freedom oscillators with elastic period, $T = 1.0$ s: (a) elastic case, 5% damping; (b) ASCE 7-10 elastic deformation limit D_y (DE/R_d), $R_d = 4$; (c) inelastic deformation demand, D_{max} , $R_d = 4$, 2% damping; (d) inelastic-damage potential (D_{max}/D_y), $R_d = 4$, 2% damping. The color version of this figure is available only in the electronic edition.

To evaluate the effect of these spatial variations in the residuals, we fit a simple model that accounts for possible azimuthal differences in path effects. The model is described as

$$Y = b_1(eq) + b_2(az) \times R_{RUP}/100, \quad (1)$$

in which Y is the total residual, b_1 is an event-specific constant for event eq , b_2 is an adjustment for the linear distance scaling that is different for different azimuthal directions (az), and R_{RUP} is in units of km. The partitioning into 12 different adjustment regions (in 30° bins) is shown in Figure 12a,b. To account for different number of data in different bins, the b_2 coefficients are modeled as random effects according to

$$b_2 \sim N(\mu_{b_2}, \sigma_{b_2}), \quad (2)$$

in which μ_{b_2} and σ_{b_2} represent the mean and standard deviation of the b_2 coefficients, respectively. We do not fit the model of equation (1) to the residuals of the ID GMM, since the applicability range of the model is shorter than the other models, which leaves less data.

The parameters of the model are estimated via Bayesian inference using the program Stan (Carpenter *et al.*, 2017). Figure 13a shows the estimated b_2 values for two directions (west-southwest, Region A; and south-southeast, Region B) using BSSA GMM residuals. At short periods, adjustments to the linear distance scaling are similar for these two regions, while they diverge for longer periods; this difference is mapped into the average event residuals. Figure 13b shows the values of σ_{b_2} (which measures the overall range across all 12 regions) against period for all GMMs, which show similar

behavior. At long periods, differences between the GMMs become larger. One possible reason for this behavior is that at long periods, basin effects become more important. Because the different GMMs have different scaling for basin effects, these differences may also potentially map into differences in residuals. Further investigation of this is beyond the scope of this article, as

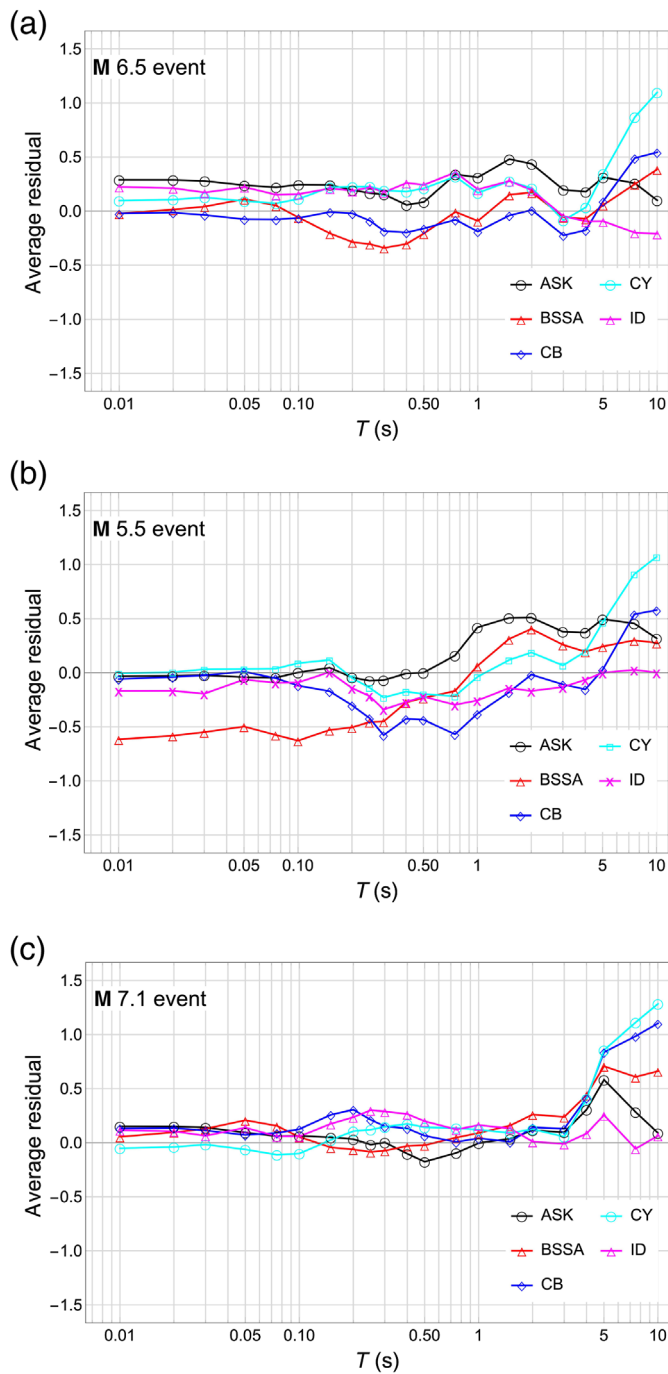


Figure 10. Event terms (average residuals) for the three Ridgecrest events (a) **M** 6.5, (b) **M** 5.5, (c) **M** 7.1 for the five NGA-West2 models versus spectral period. ASK, Abrahamson *et al.* (2014); BSSA, Boore *et al.* (2014); CB, Campbell and Bozorgnia (2014); CY, Chiou and Youngs (2014); ID, Idriss (2014). The color version of this figure is available only in the electronic edition.

it is difficult to separate site and path effects from single events (or single-source zones).

One can still calculate ergodic within-event residuals, by subtracting the average residual from the full residuals. These are shown for periods $T = 0.01, 0.2,$ and 1.0 s against

rupture distance in Figure 14. There is no clear trend in the within-event residuals. Hence, even though Figure 12a,b indicate that there are path effects in the data, on average the ergodic distance attenuation built into the NGA-West2 GMMs performs well, a conclusion also made by Parker *et al.* (2020, this issue) for the BSSA GMM. Figure 15 shows a comparison of the standard deviation of the computed within-event residuals with the published values of the within-event standard deviation. The published standard deviations are quite close to the observed ones.

ANALYSIS OF DIRECTIVITY AND HETEROGENEITY

Directivity

We investigate the role of rupture directionality and slip distribution on near-fault ground motions to quantify the impact of correcting for directivity and heterogeneity of rupture and slip on the predictions of five NGA-West2 GMMs. The Ridgecrest mainshock was recorded by 11 stations within 20 km of the source, which is considered insufficient for statistical analysis. As a result, we used 18 recordings out to 35 km distance; some prior work suggests that directivity effects can occur at these larger distances (Spudich *et al.*, 2013). In Figure 16a,b, we examine directivity using residuals for 2.0 s PSA from the CB GMM for sites with $R_{RUP} < 35$ km from the **M** 7.1 event.

We examine the near-fault data relative to the directivity-heterogeneity model of Rowshandel (2010) (also presented in Spudich *et al.*, 2013, 2014). The concepts from Rowshandel (2010) were adapted into a model for narrow-band adjustment of RotD50 response spectra by Rowshandel (2018a), with further application of model centering by Rowshandel (2018b). The Rowshandel (2010) model and other contemporary models for analysis of rupture directivity were evaluated by Donahue *et al.* (2019); although there is substantial model-to-model variability, only the Rowshandel (2010) model is considered in this article.

We apply the Rowshandel (2010) directivity-heterogeneity model using the FFM presented previously. The preferred hypocentral depth of 8 km (Tables 1 and 2) was not used. Instead, a deeper hypocenter (17 km) recommended by Dreger (2019) was used. Considering that the rupture directivity effects at the 18 near-source stations are partly due to the up-dip rupture and partly caused by the along-strike ruptures, using a shallower hypocenter would reduce model predictions from the Rowshandel (2010) model, especially for sites located at mid-length of the fault and directly above the hypocenter. Using the deeper hypocenter, we improve the model fit to the data.

We compute the Rowshandel (2010) directivity parameter (ξ ; see equation 3 in Rowshandel, 2010) for the 18 near-source stations. Table 5 provides a list of directivity parameters for these stations. The directivity parameter was then linearly correlated with ground-motion within-event residuals (δ) for the five GMMs to find event-specific directivity

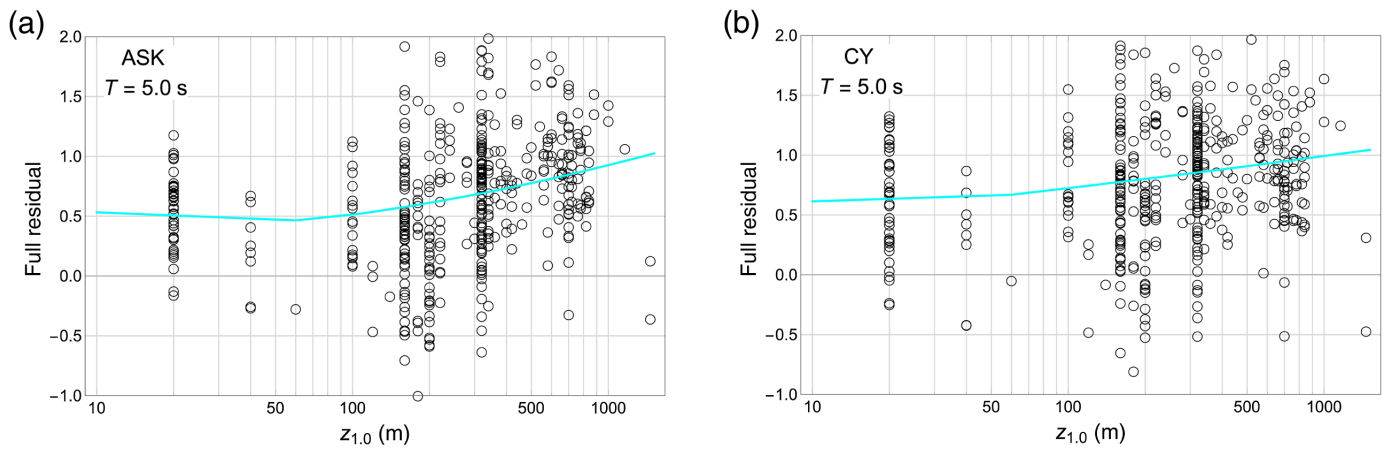


Figure 11. Total residuals for the (a) ASK and (b) CY ground-motion models (GMMs) at $T = 5.0$ s, plotted against depth to a shear-wave horizon of

1 km/s ($z_{1,0}$). The color version of this figure is available only in the electronic edition.

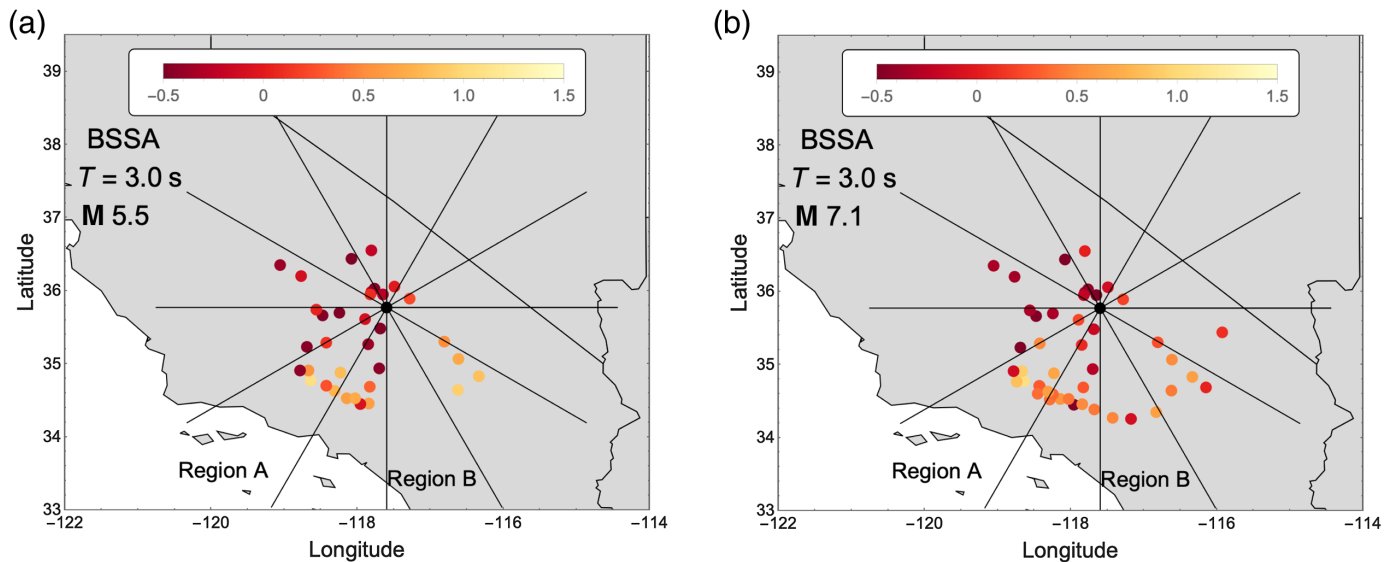


Figure 12. Spatial distribution of total residuals for the BSSA model at $T = 3.0$ s, for the (a) $M 5.5$ event and the (b) $M 7.1$ mainshock. Solid black lines show the delineation of azimuthal binned regions for

investigation of possible nonergodic path effects. The color version of this figure is available only in the electronic edition.

coefficients C_1 and C_2 at periods from 0.1 to 10 s (equation 3):

$$\delta = C_1 \xi + C_2. \quad (3)$$

We then compute and compare the dispersions of near-source ground motions at the periods given previously for all five GMMs, before correcting for directivity (ϕ) and after correcting (ϕ_c):

$$\phi = [(1/N)\Sigma(\delta_i)^2]^{1/2}, \quad (4a)$$

$$\phi_c = [(1/N)\Sigma(\delta_i - C_1 \xi - C_2)^2]^{1/2}. \quad (4b)$$

Figure 17a compares the dispersions in ground-motion residuals (ϕ and ϕ_c) for periods between 0.1 and 10 s for the five GMMs. Figure 17b represents the percent changes in the previous measures of dispersion resulting from the correction for directivity. As can be seen from Figure 17, correcting for directivity using an event-specific model, and a selected hypocenter depth different from the recommended hypocenter depths in Tables 1 and 2, reduces the dispersion

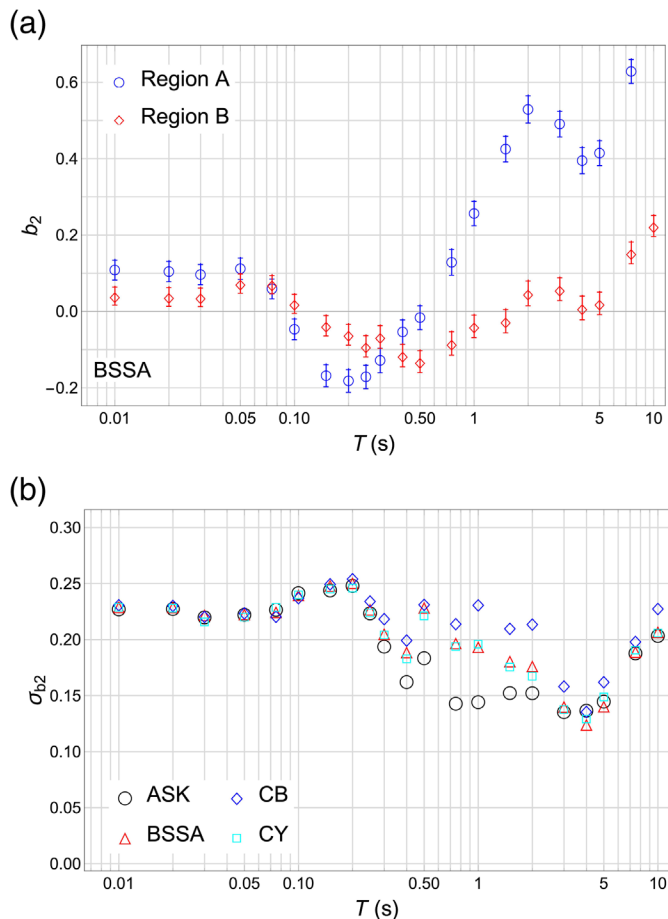


Figure 13. (a) Adjustments to linear distance scaling for two different azimuthal regions (see Fig. 12) for model BSSA. (b) Standard deviation of linear distance adjustments over all 12 regions. The color version of this figure is available only in the electronic edition.

in the ground-motion residuals by as much as 25%. We acknowledge that this correction could not be applied *a priori*, and we expect that dispersion results derived using more generic (not event-specific) models and shallower hypocenter depths would be smaller.

The results presented in Figure 17a,b reveal two period ranges of elevated dispersion, one centered around 0.3 s and the other centered near 1.5 s. It is possible that these elevated dispersion levels correspond to directivity pulses in some of the records.

Fault-slip heterogeneity

The analyses of directivity, described previously, are based on assumptions of homogenous rupture and uniform slip (i.e., an isotropic rupture initiating from the hypocenter and a constant rake angle) on the fault. These assumptions are major simplifications of source behavior. Realistically, the direction of rupture as well as the size and direction of slip vary significantly over the fault surface. Such variabilities in source rupture and

slip contribute to ground-motion variability, especially in the near-source region. The potential use of information on the size, location, and strength of asperities and data on the slip distribution of faults in developing GMMs would significantly help improve characterization and quantification of such variations of near-source ground motions.

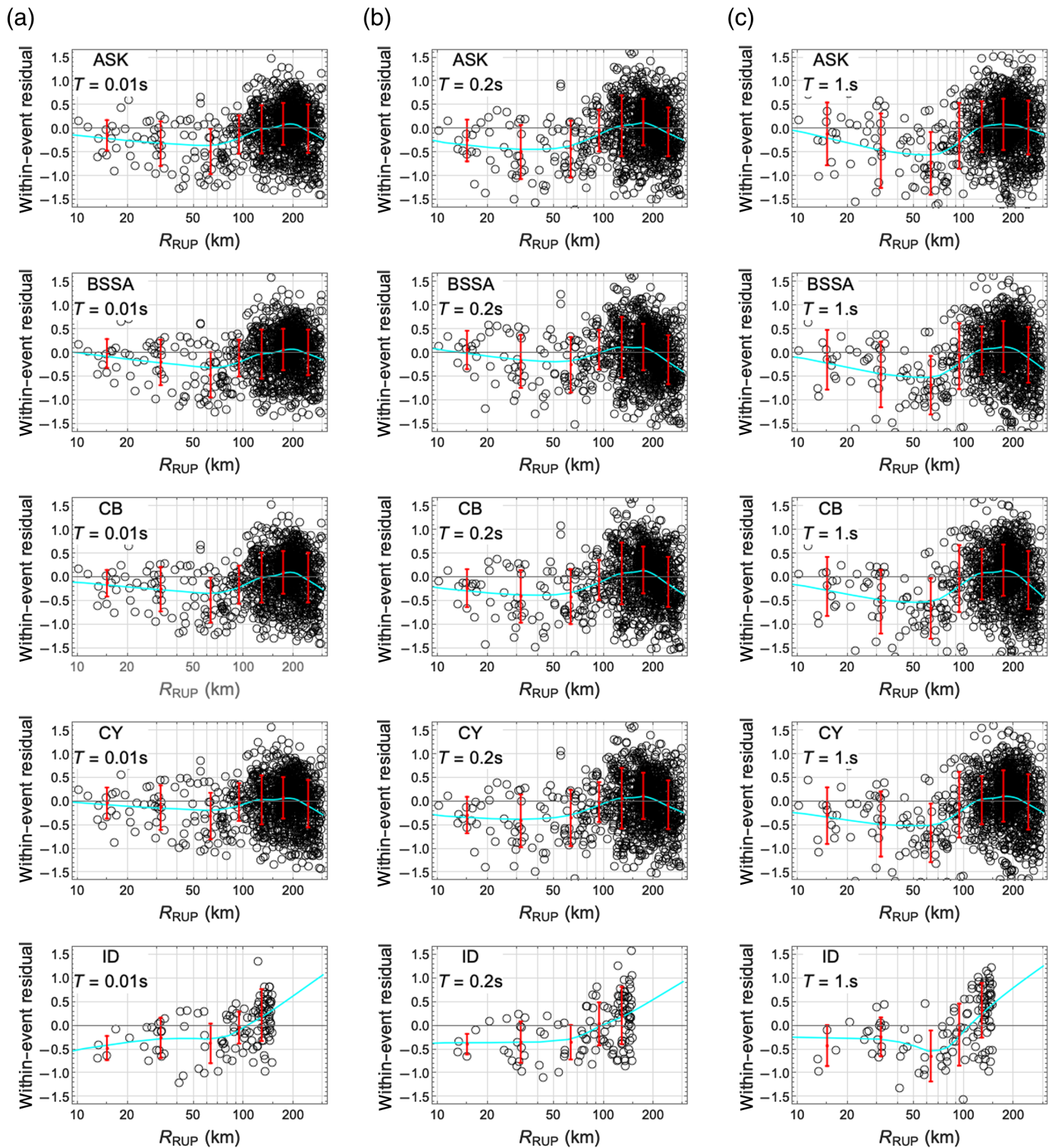
The directivity parameter used in the Rowshandel (2010) directivity-heterogeneity model addressed earlier, through the use of a single heterogeneity coefficient (called ζ in Rowshandel, 2010, equation 3), reflects to some degree these effects. A proof-of-concept analysis was performed using alternate asperity size and locations (i.e., regions of high slip) to investigate the role and the level of significance of source rupture-slip heterogeneity in the M 7.1 event. FFMs indicating locations of high slip were not considered in the present analyses; rather slip patches were placed at different locations on the fault so as to find those locations that minimize residual dispersion when GMM predictions are modified using the Rowshandel (2010) directivity model.

This approach uses definitions proposed by Somerville *et al.* (1999). Asperities, defined as regions of high slip ($\zeta \sim 3-5$) and of areas roughly 20%–30% of the total fault surface area, were placed at different locations on the fault, and the directivity analyses presented earlier (i.e., corresponding to $\zeta = 1$) were repeated. The three asperity scenarios (labeled A1, A2, and A3) and the results of the analyses for the cases of the CB and BSSA GMMs are summarized in Figure 18a–c.

As shown in Figure 18a–c, two of the three identified asperity locations reduce ground-motion dispersions, beyond what was achieved due to the homogeneous directivity correction. Placing the asperities in most other locations on the fault did not result in reductions of dispersion (these results are not shown for brevity). Figure 18c shows that the largest dispersion reduction among the three asperity locations is A2 (asperity in southeast end of fault), which differs from the location of the principle slip patch near the middle of the fault from available solutions (Xu *et al.*, 2020; Chen *et al.*, 2020). Because these asperity locations do not have a clear association with high-slip zones, and because the directivity model used in these analyses is event-specific, it is unclear to what extent this approach can reduce ground-motion dispersions in forward analyses.

SUMMARY

The 2019 Ridgecrest earthquake sequence was widely felt throughout southern and central California. Because of a dense and widespread network of seismic recording instruments, a ground-motion dataset of unprecedented size for individual events in California has been collected. Ground motions are processed using standard NGA procedures and various intensity measures are computed, including PSA at various oscillator periods and components, as well as inelastic response spectra. Future work relating to comparison of predicted



inelastic damage potentials with observed damage to various structure types is warranted, particularly if information regarding structural damage within the China Lake Naval Air Weapons Station can be obtained.

Metadata pertaining to the earthquake source such as finite-fault solutions, seismic site information, including V_{S30} and basin depths, and wave propagation path distances are compiled. We utilize a RDB to organize and store all data.

Figure 14. Within-event residuals against rupture distance for the five NGA-West2 models at three periods: (a) $T = 0.01$ s, (b) $T = 0.2$ s, and (c) $T = 1.0$ s. A loess regression (Fox, 2010) is shown with a solid line, and mean within-event residuals $\pm 1\sigma$ over distance bins are shown as vertical bars. The color version of this figure is available only in the electronic edition.

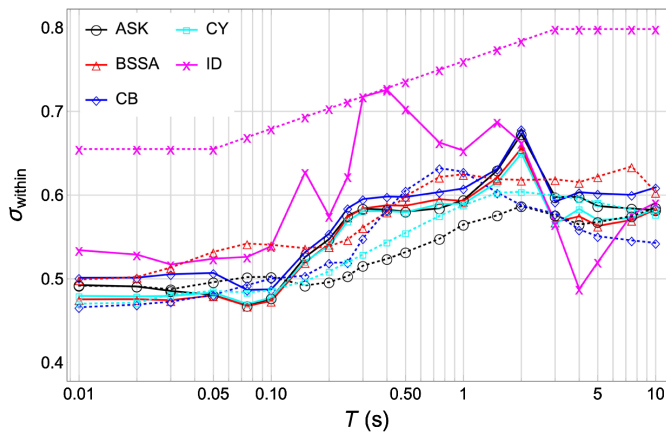


Figure 15. Standard deviation (σ_{within}) of within-event residuals (solid lines) and published value of within-event standard deviation (dashed lines) for the five NGA-West2 GMMs. The ID model does not partition the full standard deviation into within-event and between-event standard deviations; in this case, the full published standard deviation is plotted. The color version of this figure is available only in the electronic edition.

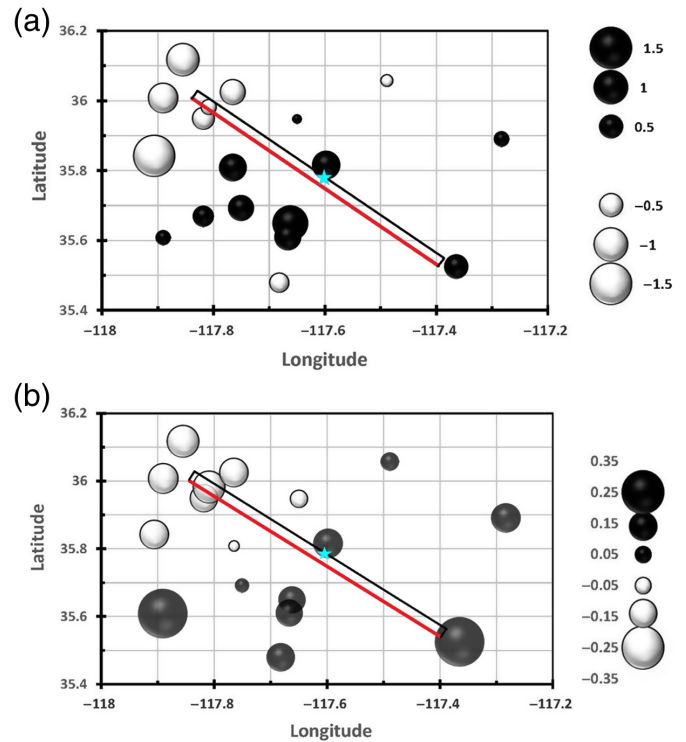


Figure 16. (a) Regional distribution of centered near-source ($R < 35$ km) within-event ground-motion residuals of Campbell and Bozorgnia (2014) model at the spectral period of 2.0 s. Full and empty circles represent positive and negative residuals (underpredicted and overpredicted ground motions), respectively, and the relative diameters of the circles indicate the sizes of the residuals. The surface projection of the **M** 7.1 fault and the hypocenter are indicated (intersection with ground surface marked in red, star indicates epicenter); (b) Regional distribution of centered directivity parameter ξ at the 18 recording stations within 35 km of the source. The color version of this figure is available only in the electronic edition.

TABLE 5

Summary of 18 Closest Stations Used in Analysis of Directivity–Heterogeneity

Station Name	Station Latitude (°)	Station Longitude (°)	R_{RUP} (km)	Residual to CB GMM (δ)*	Directivity Parameter (ξ)
CLC	35.8157	-117.598	2	0.249	0.13
CCC	35.5249	-117.365	5	0.0819	0.36
WRC2	35.9479	-117.65	8	-0.3089	-0.05
TOW2	35.8086	-117.765	10	0.2137	-0.02
5149	35.6491	-117.662	12	0.6023	0.11
WVP2	35.9494	-117.818	13	-0.7953	-0.12
JRC2	35.9825	-117.809	15	-0.5874	-0.16
Q0072	35.6096	-117.667	15	0.1823	0.11
SRT	35.6924	-117.751	16	0.1414	0.03
WCS2	36.0252	-117.765	17	-0.9152	-0.13
WNM	35.8422	-117.906	20	-1.7615	-0.13
WRV2	36.0077	-117.89	22	-1.1052	-0.14
33742	35.6696	-117.819	23	-0.0397	0
LRL	35.4795	-117.682	26	-0.7045	0.12
MPM	36.0580	-117.489	27	-0.5159	0.05
WMF	36.1176	-117.855	30	-1.2515	-0.16
SLA	35.8910	-117.283	31	-0.1958	0.13
WBM	35.6084	-117.891	32	-0.2026	0.36

CB, Campbell and Bozorgnia (2014); GMM, ground-motion model.
 *Within-event residual for CB GMM (spectral acceleration at $T = 2.0$ s).

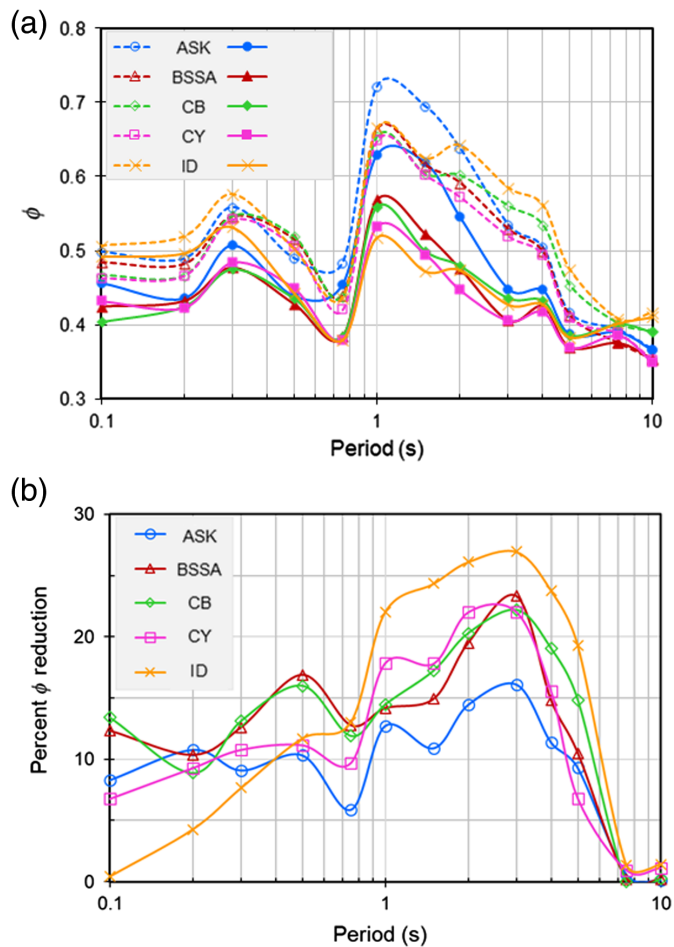


Figure 17. Dispersions of ground motion residuals at 18 near-source sites as functions of period for the five NGA-West2 GMMs; (a) the group of five broken-line curves on the top represent dispersions of the GMMs without directivity (ϕ) and the group of solid lines represent the residuals after applying an event-specific directivity modification to predicted ground motions (ϕ_c); (b) percentage reduction in the dispersions. The color version of this figure is available only in the electronic edition.

Comparisons of the recorded ground motions to NGA-West2 shallow crustal GMMs show an average favorable model performance. This is likely due to the fact that a significant portion of path data contained in the NGA-West2 database are located in southern California, which means that the California-specific path model used in the models captures relatively well the anelastic attenuation of ground motion with distance.

The Ridgecrest events are among the best-recorded events in California. As such, they have significant value for investigating specific regional effects, including azimuth-dependent path effects and regional site response (e.g., differences among basins). Moreover, they provide an excellent resource for validation of ground-motion simulations. These topics will be the subject of future research. An analysis of rupture directivity and heterogeneity effects demonstrates that the dispersion

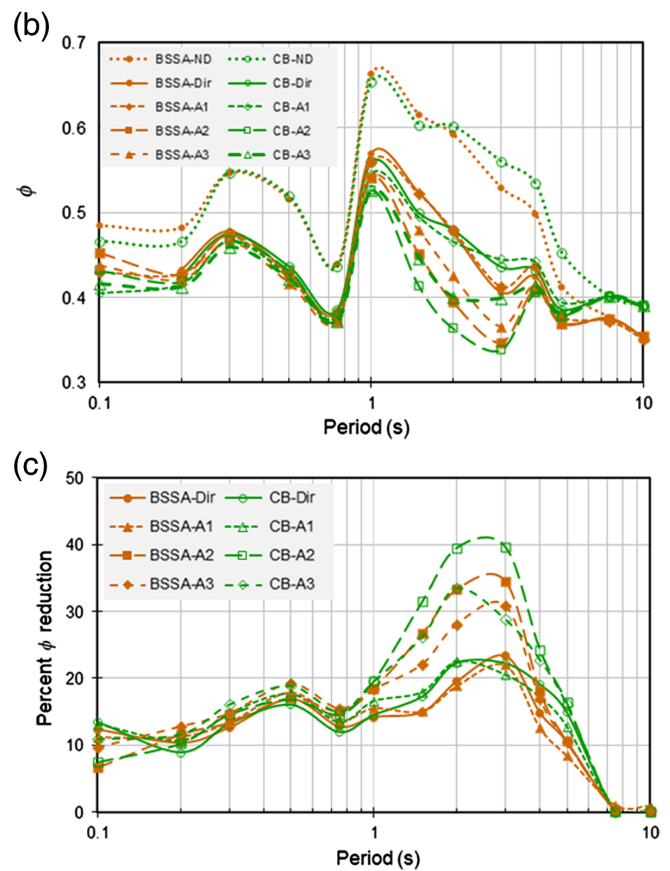
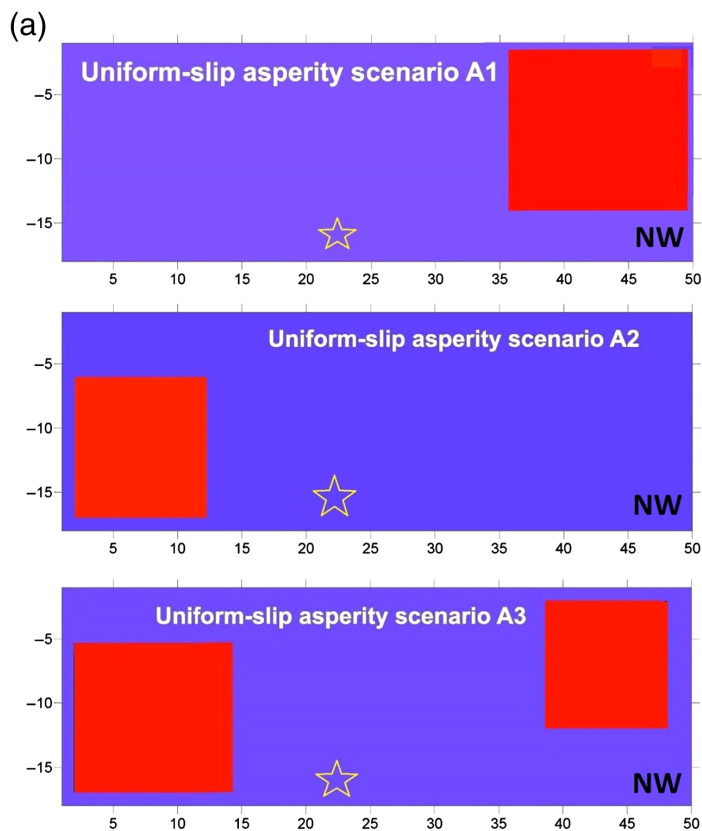
in the near-source ground-motion residuals of the M 7.1 earthquake can be reduced significantly when these factors are taken into consideration. Future work includes the inclusion of this dataset with others in southern California and shallow crustal earthquakes worldwide to update GMMs for these regions.

DATA AND RESOURCES

Recorded strong-motion data were accessed through the Center for Engineering Strong-Motion Data (CESMD, 2019). Processed data products that were developed as part of this study are available from the Natural Hazards Risk and Resiliency Research Center (NHR3) of the B. John Garrick Institute for the Risk Sciences at the University of California, Los Angeles (UCLA) Samueli School of Engineering, and described in a report by Ahdi *et al.* (2019), available at <https://www.risksciences.ucla.edu/nhr3/gmdata/2019-ridgecrest-earthquake-sequence> (last accessed January 2020). Traces of mapped regional faults presented in the maps in Figures 1, 2, 8, and 9 were obtained from the U.S. Geological Survey (USGS) Quaternary Fault and Fold Database for the United States (<https://earthquake.usgs.gov/hazards/qfaults/>, last accessed July 2019). Information on preliminary earthquake magnitudes epicentral locations, and hypocentral depths was obtained from the event pages maintained by the USGS for each earthquake (<https://www.usgs.gov/natural-hazards/earthquake-hazards/earthquakes>, last accessed January 2020). Finite-fault models for the M 6.5 and M 7.1 events were obtained in digital format from the Finite-Fault Earthquake Source Model Database (SRCMOD), available at <http://equake-rc.info/srcmod/> (last accessed January 2020). All V_{S30} and z_x data are publicly available and were obtained from the various sources, as described in the [Compilation of Metadata](#) section, including the updated V_{S30} map for California with geologic and topographic constraints published as a Data Release by the USGS (Thompson, 2018; doi: 10.5066/F7JQ108S), as is the USGS Compilation of V_{S30} data for the United States (Yong *et al.*, 2016; doi: 10.3133/ds978). The FORTRAN code “CCLD” used to simulate the fault plane of the M 5.5 event was developed by Bob Youngs and used in the Next Generation Attenuation (NGA)-West1 (Power *et al.*, 2008) and NGA-West2 (Ancheta *et al.*, 2013) Projects. The FORTRAN code “P4CF” used to compute distances was developed by Brian Chiou and used in the NGA-Subduction Project (Contreras *et al.*, 2020). Residuals to the NGA-West models are calculated using the Python package “pygmm” (Kottke, 2016). The American Society of Civil Engineers (ASCE) 7–10 risk-targeted maximum considered earthquake (MCE_R) spectrum was obtained for each recording station via the USGS Design Maps Web Services tools (<https://earthquake.usgs.gov/ws/designmaps/>, last accessed January 2020). The unpublished manuscript by Dawson, T. C., B. Du Ross, R. Gold, K. Scharer, D. Ponti, T. Ladinsky, V. E. Langenheim, D. McPhillips, A. Morelan, C. Milliner, *et al.* (2020). “Field-based observations of surface ruptures associated with the 2019 Ridgecrest earthquake sequence,” submitted to *Bull. Seismol. Soc. Am.*

ACKNOWLEDGMENTS

Support from the Pacific Gas and Electric Company (PG&E) and the California Strong Motion Instrumentation Program (CSMIP) is gratefully acknowledged. Parts of this effort were initially conducted as part of the Geotechnical Extreme Event Reconnaissance (GEER) deployment (GEER, 2019). The GEER Association is supported by



the National Science Foundation (NSF) through the Geotechnical Engineering Program under Grant Number CMMI-1266418. Any opinions, findings, and conclusions or recommendations expressed in this material are those of the authors and do not necessarily reflect those of the supporting agencies. The authors thank Ivan Wong and Emily Wolin for providing constructive feedback that helped improve this article.

REFERENCES

- Abrahamson, N. A., W. J. Silva, and R. Kamai (2014). Summary of the ASK14 ground motion relation for active crustal regions, *Earthq. Spectra* **30**, no. 3, 1025–1055.
- Ahdi, S. K., S. Mazzoni, T. Kishida, P. Wang, C. C. Nweke, J. P. Stewart, and Y. Bozorgnia (2019). *Processed ground motion recordings of the 2019 Ridgecrest earthquake sequence, Report of the Natural Hazards Risk and Resiliency Research Center (NHR3)*, B. John Garrick Institute for the Risk Sciences, University of California, Los Angeles, California, available at <https://www.risksciences.ucla.edu/nhr3/gmdata/2019-ridgecrest-earthquake-sequence> (last accessed December 2019).
- Ahdi, S. K., S. Sadiq, O. Ilhan, Y. Bozorgnia, Y. M. A. Hashash, D. Y. Kwak, D. Park, A. Yong, and J. P. Stewart (2018). Development of a United States community shear wave velocity profile database, *Selected Papers from Sessions of the 5th Conf. on Geotechnical Earthquake Engineering and Soil Dynamics (GEESD-V)*, S. J. Brandenberg and M. T. Manzari (Editors), Seismic Hazard Analysis, Earthquake Ground Motions, and Regional-Scale

Figure 18. (a) Schematic representation of the three scenarios of uniform-slip asperities investigated in proof-of-concept analysis; (b) dispersions in the near-source ($R < 35$ km) ground-motion residuals of the Campbell and Bozorgnia (2014) and Boore *et al.* (2014) GMMs as functions of period before modification (dotted curves) and after modification for directivity (solid curves) and for heterogeneity based on rupture-slip scenarios A1 through A3; (c) reductions of near-source ($R < 35$ km) ground-motion residuals of Campbell and Bozorgnia (2014) and Boore *et al.* (2014) GMMs as functions of period after modifications for directivity (solid curve) and heterogeneity (broken-line curves) based on rupture-slip scenarios A1 through A3. The color version of this figure is available only in the electronic edition.

Assessment, Geotechnical Special Publication Number 291 of the Geo-Institute of the American Society of Civil Engineers, Austin, Texas, 10–13 June, 330–339.

- American Society of Civil Engineers (ASCE) (2010). *Minimum Design Loads for Buildings and Other Structures*, ASCE/SEI 7–10, Reston, Virginia.
- Ancheta, T. D., R. B. Darragh, J. P. Stewart, E. Seyhan, W. J. Silva, B. S.-J. Chiou, K. E. Wooddell, R. W. Graves, A. R. Kottke, D. M. Boore, *et al.* (2013). *PEER NGA-West2 Database*, PEER Rept. 2013/03, Pacific Earthquake Engineering Research Center, Berkeley, California.
- ASCE (2016). *Minimum Design Loads and Associated Criteria for Buildings and Other Structures*, ASCE/SEI 7–16, Reston, Virginia.

- Boore, D. M. (2010). Orientation-independent, non geometric-mean measures of seismic intensity from two horizontal components of motion, *Bull. Seismol. Soc. Am.* **100**, no. 4, 1830–1835.
- Boore, D. M., J. P. Stewart, E. Seyhan, and G. M. Atkinson (2014). NGA-West2 equations for predicting PGA, PGV, and 5% damped PSA for shallow crustal earthquakes, *Earthq. Spectra* **30**, no. 3, 1057–1085.
- Brocher, T. M., B. T. Aagaard, R. W. Simpson, and R. C. Jachens (2006). The USGS 3D seismic velocity model for northern California, *2006 Fall Meeting, American Geophysical Union (AGU)*, San Francisco, California, 11–15 December, Abstract S51B–1266.
- Campbell, K. W., and Y. Bozorgnia (2014). NGA-West2 ground motion model for the average horizontal components of PGA, PGV, and 5% damped linear acceleration response spectra, *Earthq. Spectra* **30**, no. 3, 1087–1115.
- Carpenter, B., A. Gelman, M. D. Hoffman, D. Lee, B. Goodrich, M. Betancourt, M. Brubaker, J. Guo, P. Li, and A. Riddell (2017). Stan: A probabilistic programming language, *J. Stat. Software* **76**, no. 1, 1–32, doi: [10.18637/jss.v076.i01](https://doi.org/10.18637/jss.v076.i01).
- CESMD (2019). Center for engineering strong motion data, <https://strongmotioncenter.org/> (last accessed December 2019).
- Chen, P., and E. J. Lee (2017). UCVm 17.3.0 documentation, available at <http://hypocenter.usc.edu> (last accessed January 2020).
- Chen, K., J.-P. Avouac, A. Aati, C. Milliner, F. Zheng, and C. Shi (2020). Cascading and pulse-like ruptures during the 2019 Ridgecrest earthquakes in the eastern California shear zone, *Nat. Commun.* **11**, doi: [10.1038/s41467-019-13750-w](https://doi.org/10.1038/s41467-019-13750-w).
- Chiou, B. S.-J., and R. R. Youngs (2008). *NGA Model for Average Horizontal Component of Peak Ground Motion and Response Spectra*, PEER Rept. 2008/09, Pacific Earthquake Engineering Research Center, Berkeley, California.
- Chiou, B. S.-J., and R. R. Youngs (2014). Update of the Chiou and Youngs NGA model for the average horizontal component of peak ground motion and response spectra, *Earthq. Spectra* **30**, no. 3, 1117–1153.
- Cochran, E. S., E. Wolin, D. E. McNamara, A. Yong, D. Wilson, M. Alvarez, N. van der Elst, A. McClain, and J. H. Steidl (2020). The U.S. Geological Survey's rapid seismic array deployment for the 2019 Ridgecrest earthquake sequence, *Seismol. Res. Lett.* doi: [10.1785/0220190296](https://doi.org/10.1785/0220190296).
- Contreras, V., J. P. Stewart, T. Kishida, R. B. Darragh, B. S.-J. Chiou, S. Mazzoni, N. Kuehn, S. K. Ahdi, K. Wooddell, R. R. Youngs, et al. (2020). Source and path database, in *Data Resources for NGA-Subduction Project*, J. P. Stewart (Editor), Chapter 4, PEER Rept. 2020/02, Pacific Earthquake Engineering Research Center, UC Berkeley, Berkeley, California.
- Cox, B. R., and A. N. Beekman (2011). Intramethod variability in ReMi dispersion measurements and V_S estimates at shallow bedrock sites, *J. Geotech. Geoenviron. Eng.* **137**, no. 4, 354–362.
- Donahue, J. L., J. P. Stewart, N. Gregor, and Y. Bozorgnia (2019). *Ground-Motion Directivity Modeling for Seismic Hazard Applications*, PEER Rept. 2019/03, Pacific Earthquake Engineering Research Center, Berkeley, California.
- Dreger, D. (2019). July 2019 03:19:52 UTC 6.9 Ridgecrest, CA, available at https://ds.iris.edu/media/specialevent/2019/07/04/central-california/ucb_finitesource_model_07062019.pdf (last accessed December 2019).
- Ekström, G., M. Nettles, and A. M. Dziewonski (2012). The Global CMT project 2004–2010: Centroid-moment tensors for 13,017 earthquakes, *Phys. Earth Planet. In.* **200/201**, 1–9.
- Ely, G. P., T. H. Jordan, P. Small, and P. J. Maechling (2010). A V_{S30} -derived near-surface seismic velocity model, *2010 Fall Meeting AGU*, San Francisco, California, Abstract S51A-1907.
- Ely, G., P. Small, T. Jordan, P. Maechling, and F. Wang (2016). A V_{S30} -derived near-surface seismic velocity model, available at <http://elygeo.net/Vs30GTL-Ely+4-2016.html> (last accessed December 2019).
- Fox, J. (2010). *Nonparametric Regression in R: An Appendix to an R Companion to Applied Regression*, Second Ed., SAGE Publications, Inc., Thousand Oaks, California, revised December 2010.
- GEER (2019). 2019 Ridgecrest earthquake sequence, Geotechnical Extreme Event Reconnaissance (GEER) Association Rept. GEER-064, doi: [10.18118/G6H66K](https://doi.org/10.18118/G6H66K).
- Goulet, C. A., T. Kishida, C. H. Cramer, R. B. Darragh, W. J. Silva, Y. M. A. Hashash, J. Harmon, J. P. Stewart, K. E. Wooddell, and R. R. Youngs (2014). *PEER NGA-East Database*, PEER Rept. 2014/09, Pacific Earthquake Engineering Research Center, Berkeley, California.
- Graves, R. W., and A. Pitarka (2010). Broadband ground-motion simulation using a hybrid approach, *Bull. Seismol. Soc. Am.* **100**, 2095–2123.
- Hauksson, E. (2010). Crustal structure and seismic distribution adjacent to the Pacific and North America plate boundary in southern California, *J. Geophys. Res.* **105**, no. B6, 13,875–13,903.
- Idriss, I. M. (2014). An NGA-West2 empirical model for estimating the horizontal spectral values generated by shallow crustal earthquakes, *Earthq. Spectra* **30**, no. 3, 1155–1177.
- Iwahashi, J., and R. J. Pike (2007). Automated classifications of topography from DEMs by an unsupervised nested-means algorithm and a three-part geometric signature, *Geomorphology* **86**, 409–440.
- Kishida, T., R. B. Darragh, B. S.-J. Chiou, Y. Bozorgnia, S. Mazzoni, V. Contreras, R. Boroschek, F. Rojas, and J. P. Stewart (2020). Ground motions and intensity measures, in *Data Resources for NGA-Subduction Project*, J. P. Stewart (Editor), Chapter 3, PEER Rept. 2020/20, Pacific Earthquake Engineering Research Center, UC Berkeley, Berkeley, California.
- Kishida, T., O. Ktenidou, R. B. Darragh, and W. J. Silva (2016). *Semi-Automated Procedure for Windowing Time Series and Computing Fourier Amplitude Spectra for the NGA-West2 Database*, PEER Rept. 2016/02, Pacific Earthquake Engineering Research Center, Berkeley, California.
- Kohler, M. D., H. Magistrale, and R. W. Clayton (2003). Mantle heterogeneities and the SCEC reference three-dimensional seismic velocity model version 3, *Bull. Seismol. Soc. Am.* **93**, 757–774.
- Kottke, A. (2016). pygmm: Ground motion models implemented in Python (Version 0.4.1), *Zenodo*, doi: [10.5281/zenodo.53814](https://doi.org/10.5281/zenodo.53814).
- Lee, E. J., P. Chen, T. H. Jordan, P. J. Maechling, M. Denolle, and G. C. Beroza (2014). Full-3-D tomography for crustal structure in southern California based on the scattering-integral and the adjoint wavefield methods, *J. Geophys. Res.* **119**, 6421–6451.

- Louie, J. N. (2001). Faster, better: Shear-wave velocity to 100 meters depth from refraction microtremor arrays, *Bull. Seismol. Soc. Am.* **91**, no. 2, 347–364.
- Mai, P. M., and K. K. S. Thingbaijam (2014). SRCMOD: An online database of finite-fault rupture models, *Seismol. Res. Lett.* **85**, no. 6, 1348–1357.
- Mazzoni, S., T. Kishida, S. K. Ahdi, V. Contreras, R. B. Darragh, B. S.-J. Chiou, N. Kuehn, Y. Bozorgnia, and J. P. Stewart (2020). Relational database, in *Data Resources for NGA-Subduction Project*, J.P. Stewart (Editor), Chapter 2, PEER Rept. 2020/20, Pacific Earthquake Engineering Research Center, UC Berkeley, Berkeley, California.
- McKenna, F., M. H. Scott, and G. L. Fenves (2010). Nonlinear finite-element analysis software architecture using object composition, *J. Comput. Civ. Eng.* **24**, no. 1, 95–107.
- Nweke, C. C., P. Wang, S. J. Brandenberg, and J. P. Stewart (2018). Reconsidering basin effects in ergodic site response models, *Proc. of the 2018 California Strong Motion Instrumentation Program (CSMIP) Seminar on Utilization of Strong-Motion Data*, Sacramento, California, 25 October.
- Parker, G. A., A. S. Baltay, J. Rekoske, and E. M. Thompson (2020). Repeatable Source, Path, and Site Effects from the 2019 M7.1 Ridgecrest Earthquake Sequence, *Bull. Seismol. Soc. Am.* doi: [10.1785/0120200008](https://doi.org/10.1785/0120200008).
- Power, M., B. Chiou, N. Abrahamson, Y. Bozorgnia, T. Shantz, and C. Roblee (2008). An overview of the NGA Project, *Earthq. Spectra* **24**, no. 1, 3–21.
- Ross, Z. E., B. Idini, Z. Jia, O. L. Stephenson, M. Zhong, X. Wang, Z. Zhan, M. Simons, E. J. Fielding, S. H. Yun, and E. Hauksson (2019). Hierarchical interlocked orthogonal faulting in the 2019 Ridgecrest earthquake sequence, *Science* **366**, no. 6463, 346–351.
- Rowshandel, B. (2010). Directivity correction for the Next Generation Attenuation (NGA) relations, *Earthq. Spectra* **26**, no. 2, 525–559.
- Rowshandel, B. (2018a). Directivity centering of GMPEs and of directivity models, *Eleventh U.S. National Conf. on Earthquake Engineering (11NCEE)*, Los Angeles, California, 25–29 June.
- Rowshandel, B. (2018b). Capturing and PSHA implementation of spatial variability of near-source ground motion hazards, S. J. Brandenberg and M. T. Manzari (Editors), *Selected Papers from Sessions of the 5th Conf. on Geotechnical Earthquake Engineering and Soil Dynamics (GEESD-V)*, Austin, Texas, 10–13 June.
- Seyhan, E., J. P. Stewart, T. D. Ancheta, R. B. Darragh, and R. W. Graves (2014). NGA-West2 site database, *Earthq. Spectra* **30**, 1007–1024.
- Shaw, J. H., A. Plesch, C. Tape, M. P. Suess, T. H. Jordan, G. Ely, E. Hauksson, J. Tromp, T. Tanimoto, R. W. Graves, et al. (2015). Unified structural representation of the southern California crust and upper mantle, *Earth Planet. Sci. Lett.* **415**, 1, doi: [10.1016/j.epsl.2015.01.016](https://doi.org/10.1016/j.epsl.2015.01.016).
- Small, P., D. Gill, P. J. Maechling, R. Taborda, S. Callaghan, T. H. Jordan, G. P. Ely, K. B. Olsen, and C. A. Goulet (2017). The SCEC Unified Community Velocity Model software framework, *Seismol. Res. Lett.* **88**, no. 5, 1539–1552.
- Somerville, P. (2002). Characterizing near fault ground motion for the design and evaluation of bridges, *Proc. of the Third National Seismic Conf. and Workshop on Bridges and Highways: Advances in Engineering and Technology for the Seismic Safety of Bridges in the New Millennium*, Portland, Oregon, 28 April–1 May.
- Somerville, P., K. Irikura, R. Graves, S. Sawada, D. Wald, N. Abrahamson, Y. Iwasaki, T. Kagawa, N. Smith, and A. Kowada (1999). Characterizing crustal earthquake slip models for prediction of strong ground motion, *Seismol. Res. Lett.* **7**, 59–80.
- Spudich, P., J. Bayless, J. Baker, B. Chiou, B. Rowshandel, S. Shahi, and P. Somerville (2013). *Final Report of the NGA-West2 Directivity Working Group*, PEER Rept. 2013/09, Pacific Earthquake Engineering Research Center, Berkeley, California.
- Spudich, P., B. Rowshandel, S. K. Shahi, J. W. Baker, and B. S.-J. Chiou (2014). Comparison of NGA-West2 directivity models, *Earthq. Spectra* **30**, no. 3, 1199–1221.
- Strobbia, C., and G. Cassiani (2011). Refraction microtremors: Data analysis and diagnostics of key hypotheses, *Geophysics* **76**, no. 3, 11–20.
- Süss, M. P., and J. H. Shaw (2003). P wave seismic velocity structure derived from sonic logs and industry reflection data in the Los Angeles basin, California, *J. Geophys. Res.* **108**, no. B3, 2170, doi: [10.1029/2001JB001628](https://doi.org/10.1029/2001JB001628).
- Taborda, R., S. Aizzadeh-Roodpish, N. Khoshnevis, and K. Cheng (2016). Evaluation of the southern California seismic velocity models through simulation of recorded events, *Geophys. J. Int.* **205**, no. 3, 1342–1364.
- Thompson, E. M. (2018). An updated V_{S30} map for California with geologic and topographic constraints, *U.S. Geological Survey Data Release*, doi: [10.5066/F7JQ108S](https://doi.org/10.5066/F7JQ108S).
- Thompson, E. M., D. J. Wald, and C. B. Worden (2014). A V_{S30} map for California with geologic and topographic constraints, *Bull. Seismol. Soc. Am.* **104**, 2313–2321.
- Wald, D. J., and T. I. Allen (2007). Topographic slope as a proxy for seismic site conditions and amplification, *Bull. Seismol. Soc. Am.* **97**, 1379–1395.
- Wills, C. J., C. I. Gutierrez, F. G. Perez, and D. M. Branum (2015). A next generation V_{S3} map for California based on geology and topography, *Bull. Seismol. Soc. Am.* **105**, 3083–3091.
- Worden, C. B., and D. J. Wald (2016). ShakeMap Manual Online: Technical manual, user's guide, and software guide, *U.S. Geol. Surv.* available at usgs.github.io/shakemap (last accessed December 2019).
- Xu, X., D. T. Sandwell, and B. Smith-Konter (2020). Coseismic displacements and surface fractures from Sentinel-1 InSAR: 2019 Ridgecrest earthquakes, *Seismol. Res. Lett.* **XX**, 1–7, doi: [10.1785/0220190275](https://doi.org/10.1785/0220190275).
- Yong, A. (2016). Comparison of measured and proxy-based V_{S30} values in California, *Earthq. Spectra* **32**, 171–192.

Manuscript received 18 January 2020

Published online 21 July 2020